Variation in Synaptic Inputs Drives Functional Versatility for Sound Encoding in Globular Bushy Cells

(Abbreviated title): Synaptic Input Variation in Globular Bushy Cells

Chunjian Wang[1,2], Go Ashida[3,4], Christian Keine[1,2], Ivan Milenkovic[1,2,4]

[1]Department of Human Medicine, Carl von Ossietzky Universität Oldenburg, Germany
[2]Research Center Neurosensory Science, Carl von Ossietzky Universität Oldenburg, Germany
[3]Department of Neuroscience, Carl von Ossietzky Universität Oldenburg, Germany
[4]Cluster of Excellence "Hearing4all", Carl von Ossietzky Universität Oldenburg, Germany

ORCIDs:

Chunjian Wang	0000-0002-3399-3489
Go Ashida:	0000-0002-8886-1213
Christian Keine:	0000-0003-0995-9667
Ivan Milenkovic:	0000-0003-1431-9031

Summary

Synaptic convergence is fundamental to neuronal circuit function, enabling diverse processing such as coincidence detection and reliable signal transmission. In sensory systems, the architecture of convergence and strengths of synaptic inputs are pivotal for extracting distinct features of the sensory stimulus. In auditory system, globular bushy cells (GBC) in the cochlear nucleus receive multiple axosomatic endbulb of Held terminals from the auditory nerves, which vary considerably in size, even among inputs targeting the same cell. However, the functional consequences of this input strength variation for sound encoding remain unclear. Here, we investigated how synaptic input variation shapes sound encoding in GBC of Mongolian gerbils, using in vitro conductance-clamp recordings and computational modeling, in which synaptic inputs with varying strengths were simulated. We found that input variation critically shapes GBC sound encoding by influencing temporal precision and firing rates. Low input variation allows GBC to act as coincidence detectors, thereby improving temporal precision. Conversely, high input variation increases overall firing rates and enhances the encoding of amplitude modulations, albeit at the expense of temporal precision. These findings suggest that inherent endbulb strength heterogeneity allows GBC to operate along a functional continuum. This variation in input strength may provide the basis for generating diverse information streams to downstream targets including the medial nucleus of the trapezoid body (MNTB).

Keywords: Cochlear nucleus; globular bushy cells; temporal precision; endbulb of Held; coincidence detection; conductance-clamp; auditory nerve; Mongolian gerbil; auditory brainstem; functional heterogeneity; computational modeling

Introduction

Neuronal circuits rely on intricate patterns of synaptic communication to process information and guide behavior. A core organizational principle of these circuits is synaptic convergence, where individual neurons integrate inputs from multiple presynaptic sources. The extent of such convergence varies considerably across neuron types and brain regions, reflecting distinct operational modes tailored to specific computational needs.

This diversity is particularly evident in sensory systems, where parallel pathways are often specialized to extract distinct stimulus features (Blackburn and Sachs, 1989; Nagayama et al., 2004; Doucet and Ryugo, 2006; Huang and Chacron, 2016; Ashida et al., 2019). For instance, within the auditory brainstem, the degree of synaptic convergence varies dramatically. Neurons in the medial nucleus of the trapezoid body (MNTB) are innervated by a single massive axosomatic terminal – the calyx of Held – which ensures fast and reliable signal transmission (Spirou et al., 1990; Smith et al., 1998; von Gersdorff and Borst, 2002; Schneggenburger and Forsythe, 2006; Englitz et al., 2009; Borst and Soria van Hoeve, 2012). In contrast, octopus and D-stellate cells in the cochlear nucleus (CN) integrate inputs from dozens of auditory nerve (AN) fibers, responding to the coincident firing of their inputs (Oertel, 1999; Cao and Oertel, 2010; McGinley et al., 2012; Xie and Manis, 2017; Kreeger et al., 2025). Such heterogeneity in input number also occurs among cells of the same type. For instance, retinal ganglion cells (RGCs) in the primate fovea receive input from only a few bipolar cells, whereas peripheral RGCs integrate signals from hundreds of inputs (Calkins et al., 1994; Jacoby et al., 2000; Kolb and Marshak, 2003). Similarly, in the avian CN homolog, the nucleus magnocellularis, neurons processing low-frequency sounds receive numerous small inputs, while high-frequency neurons are innervated by fewer, larger inputs (Köppl, 1994; Fukui and Ohmori, 2004), enabling frequency-dependent specialization of temporal processing (Oline et al., 2016). These examples illustrate how convergence patterns can be finely tuned to match specific functional requirements across diverse neural systems.

Beyond input number, the variation in synaptic strength among converging inputs represents another critical, yet less understood, factor influencing neuronal circuit function (Sherman and Guillery, 1998; Rouiller and Welker, 2000; Groh et al., 2008; Wolff et al., 2021; Govindaiah et al., 2023). In multiple brain regions, including the cerebellum, thalamus, and cortex, some neurons integrate many similarly sized subthreshold inputs, while others are driven by one or two suprathreshold “driver inputs” alongside multiple weaker ones (Sherman and Guillery, 1998; Groh et al., 2008; Wolff et al., 2021). Understanding how such variations in synaptic strength affect neuronal processing is essential for deciphering neural circuit computations and understanding the fundamental aspects of sensory operation.

In this study, we used globular bushy cells (GBC) in the mammalian CN as a model system to explore the functional consequences of synaptic input variation. GBC, located near the AN root in the caudal anteroventral (AVCN) and posteroventral CN (PVCN) (Osen, 1969; Cant and Morest, 1979), receive excitatory inputs via large endbulb of Held terminals from a varying number of AN fibers, ranging from 5-12 in mice (Cao and Oertel, 2010; Spirou et al., 2023) to over 20 in cats (Liberman, 1991; Ostapoff and Morest, 1991; Spirou et al., 2005). Functionally, GBC are crucial for high-fidelity temporal processing of auditory information, and their temporal precision can exceed that of AN inputs (Blackburn and Sachs, 1989; Joris et al., 1994; Wei et al., 2017). Recent detailed morphological analysis has revealed significant heterogeneity in the size of endbulbs converging onto individual GBC with some receiving inputs from many similarly sized subthreshold endbulbs, while others are dominated by a few large suprathreshold endbulbs alongside smaller ones (Nicol and Walmsley, 2002; Spirou et al., 2023). Despite this documented morphological heterogeneity, the computational role of endbulb input variation in shaping GBC output during sound processing remains poorly understood.

To address this knowledge gap, we combined *in vitro* whole-cell conductance-clamp recordings from GBC in Mongolian gerbils with computational modeling. By systematically manipulating the

variation in synaptic input strength among simulated AN fibers, we assessed its impact on GBC firing rates and temporal precision. Our findings reveal that the degree of input variation shapes GBC output characteristics. Specifically, while overall firing rates increased with input strength variation, temporal precision in encoding the stimulus fine-structure deteriorated. These findings suggest that the inherent morphological diversity of endbulb inputs plays a key role in regulating GBC encoding strategies and may contribute to the control of information flow to multiple sound processing circuits in the downstream regions of the auditory brainstem.

Results

Synaptic input variation enhances GBC firing but reduces temporal precision

To study the impact of synaptic input variation in GBC, we targeted them using their established anatomical and electrophysiological characteristics. Located in the caudal AVCN near the AN root and PVCN (Osen, 1969), GBC are characterized by round-to-oval cell bodies with a few short dendrites and typically fire only one or a few action potentials (APs) in response to suprathreshold current injection (Fig. 1A). Functionally, GBC are specialized for high-fidelity temporal processing of auditory information, often exceeding the temporal precision of their AN inputs, and can sustain high firing rates up to a few hundred spikes per second for low-frequency sound stimulation (Joris et al., 1994; Wei et al., 2017, 2023).

Using an established auditory periphery model (Bruce et al., 2018), we generated spike trains for 10 converging AN fibers responding to 200-ms pure tones (10 repetitions) at frequencies of 350 Hz, 1 kHz, and 3.5 kHz. These frequencies were chosen to encompass the range where AN fibers exhibit significant phase-locking (350 and 1000 Hz) and to extend beyond the typical upper limit, where phase-locking diminishes in rodents (Wei et al., 2017, 2023). The resulting AN spike trains were convolved with an experimentally derived EPSC waveform to generate conductance trains, which were then injected into the recorded GBC. By systematically varying the synaptic input strength distribution across these 10 simulated AN fibers, we created three distinct conditions: ‘no variation’ (all inputs of equal strength: coefficient of variation v = 0), ‘medium variation’ (v = 0.4), and ‘high variation’ (v = 1) (Fig. 1B). For the ‘high variation’ condition, the largest input was near or above the spike threshold, while for the ‘no’ and ‘medium’ variation condition, all inputs were subthreshold.

First, we analyzed how input variation affected average firing rates. We found that increasing input variation elevated GBC firing rates during stimulation at 1 kHz and 3.5 kHz (1 kHz: no variation 132 ± 48 Hz vs. high variation 171 ± 34 Hz, p = 7.9e-6, n = 15), while firing rates were moderately

134 decreased by higher input variation during 350 Hz stimulation (no variation = 245 ± 52 Hz vs. high
135 variation = 228 ± 39 Hz, p = 0.01, Fig. 1C1).

136 Next, we assessed the impact of input variation on temporal precision, quantified by vector
137 strength (VS), which measures the neuron's ability to phase-lock to the periodic waveform of an
138 acoustic stimulus. The simulated AN inputs exhibited VS values of 0.75 and 0.77 at stimulation
139 frequencies of 350 and 1000 Hz, respectively, consistent with *in vivo* observations (Johnson, 1980;
140 Palmer and Russell, 1986; Heeringa et al., 2020; Heeringa, 2024). In postsynaptic GBC, robust
141 phase-locking was observed at 350 Hz and 1 kHz but not at 3.5 kHz, in line with *in vivo* data (Wei
142 et al., 2017). Notably, increasing input variation led to a significant reduction in GBC phase-
143 locking, an effect that was particularly robust at 350 Hz (main effect variation: p = 3.7e-6; 350 Hz:
144 no variation = 0.86 ± 0.02 vs. high variation = 0.81 ± 0.01, p = 3.3e-8, Fig. 1C2). These results
145 indicate that higher input variation leads to a trade-off between increasing firing rates and
146 degrading temporal precision.

147 **Effects of input variation are well reproduced in a coincidence-counting model**

148 To investigate whether these experimental observations could be generalized and to ascertain if
149 they arose primarily from the input statistics, we employed a computational model for GBC, which
150 was first developed for cats and adapted for gerbils in the present study (Ashida et al., 2019). This
151 model generates an output spike when the summed inputs exceed an adaptive threshold. The
152 model was driven with simulated AN spike trains identical to those used in the *in vitro* experiments.
153 A wider configuration of input variations was adopted, including the 'no', 'medium', and 'high'
154 variations tested in our conductance-clamp experiments (Fig. 2A). Notably, the model reproduced
155 the key experimental findings, namely increased firing rates (Fig. 2B) and reduced temporal
156 precision with higher input variation (Fig. 2C). This suggests that the interaction between the
157 synaptic input statistics and a simplified cellular integration mechanism is sufficient to replicate the
158 experimentally observed phenomena.

159

160 **Higher input variation shortens AP latency but increases temporal jitter**

161 Given that increased synaptic input variation enhances overall firing rates (Fig. 1C1), we next
162 investigated whether this effect differentially impacts the onset and sustained phases of GBC
163 responses. To isolate these components, we constructed peristimulus time histograms (PSTH)
164 from responses to 200 repetitions of a 3.5 kHz pure-tone stimulus, a frequency selected to
165 minimize confounding phase-locking effects. Consistent with *in vivo* recordings (Britt and Starr,
166 1976; Ritz and Brownell, 1982; Blackburn and Sachs, 1989), both the simulated AN inputs and
167 GBC responses exhibited primary-like PSTHs, characterized by a sharp onset peak followed by
168 adaptation to a lower sustained rate (Fig. 3A). In addition, the PSTH exhibited a 'notch' with lower
169 activity immediately following the onset peak, which is characteristic for GBC (Smith and Rhode,
170 1987; Blackburn and Sachs, 1989) A qualitative comparison of the 'no variation' and 'high
171 variation' conditions indicated that higher input variation tended to reduce peak onset firing while
172 elevating the sustained rate (Fig. 3A2 inset). Quantitative analysis confirmed these distinct effects.
173 Onset spike probability, defined as the fraction of trials with at least one spike within the initial
174 1.5 ms of the response, was generally high but significantly decreased with increasing input
175 variation (no variation = 0.97 ± 0.02 vs. high variation = 0.94 ± 0.02, p = 7.3e-5, n = 17, Fig. 3B2).
176 Conversely, both sustained (100–200 ms) and spontaneous firing rates significantly increased
177 with higher input variation (sustained: no variation = 72 ± 27 Hz vs. high variation = 131 ± 28 Hz,
178 p = 3.2e-11, Fig. 3B3; spontaneous: no variation = 25 ± 14 Hz vs. high variation = 65 ± 15 Hz,
179 p = 4.9e-11, Fig. 3B4). To further probe the reliability and timing of the response onset, we
180 analyzed first-spike latency and jitter. Visual inspection of superimposed spikes suggested that
181 while some initial spikes occurred earlier under the 'high variation' condition, their timing across
182 repetitions appeared more variable compared to responses generated with no input variation (Fig.
183 3B1). Indeed, quantitative analysis confirmed that the average first-spike latency significantly
184 decreased with higher input variation (Fig. 3B5, no variation = 3 ± 0.14 ms vs. high variation =

185 2.92 ± 0.15 ms, p = 0.007). However, this shorter latency was accompanied by reduced temporal
186 precision, as evidenced by a significant increase in first-spike jitter (Fig. 3B6, no variation =
187 0.42 ± 0.12 ms vs. high variation = 0.63 ± 0.21 ms, p = 7.4e-5). These experimental findings were
188 replicated in the computational model (Fig. 3C) which reproduced the characteristic PSTH shapes
189 (Fig 3A3) and provided additional insight. While most response characteristics changed gradually,
190 the median spontaneous rate increased sharply at input variations of 0.7-0.8 (Fig. 3C4),
191 corresponding to the point where the largest input transitions from subthreshold to suprathreshold,
192 enabling it to generate GBC spikes on its own. The slight decrease in first-spike latency and the
193 increased first-spike jitter were also observed in the model and comparable to the experimental
194 results (Fig. 3C5, 3C6). However, the simulated distributions of first-spike latency and jitter were
195 narrower than those of the experimental data, likely due to the existence of various additional
196 noise sources in the experimental setting that were not included in the model (e.g., channel and
197 thermal fluctuations). In summary, both experimental and modeling results demonstrated that
198 input variability differentially sculpts GBC responses by enhancing sustained firing rates while
199 simultaneously degrading both the reliability and temporal precision of the response onset.

200

201 **Input variation enhances firing rate tracking of amplitude-modulated sounds**

202 The results from pure-tone stimulation suggest that the degree of synaptic input variation can
203 modulate GBC function, potentially shifting its operational emphasis: low input variation favors
204 high temporal precision, whereas high input variation enhances firing rates. To further explore this
205 phenomenon in the context of more complex, naturalistic stimuli, we examined how input variation
206 impacts the encoding of sinusoidal amplitude-modulated (SAM) sounds, which mimic the temporal
207 fluctuations present in speech and environmental sounds (Van Tasell et al., 1987; Drullman et al.,
208 1996; Joris et al., 2004). Effective SAM encoding requires both precise spike timing relative to the
209 modulation cycle (temporal code) and the ability of firing rates to track changes in sound level

(rate code). GBC are known to effectively follow rapid amplitude modulations (Palmer et al., 1986; Rhode and Greenberg, 1994; Wang and Sachs, 1994).

We simulated the spiking responses of AN fibers to a 13 kHz pure-tone carrier, 100% amplitude-modulated at frequencies of 200 Hz, 600 Hz, and 2000 Hz. Consistent with previous in vivo observations (Smith and Brachman, 1980; Joris and Yin, 1992), the firing rates of simulated AN fibers were modulated by the stimulus envelope (Fig. 4A1). This envelope phase-locking was evident for 200 and 600 Hz, but not at 2000 Hz. Injecting the corresponding conductance trains into GBC under no, medium, and high variation conditions yielded robustly modulated firing rates (Fig. 4A2), which were also reproduced by the GBC model (Fig. 4A3). In both the experimental data and the model, responses appeared qualitatively sharper and more temporally restricted under the 'no variation' condition compared to the 'high variation' condition.

Consistent with our pure-tone data, overall firing rates during SAM stimulation significantly increased with input variation for all tested modulation frequencies (main effect of variation: $p = 3e-10$; 600 Hz: no variation = 67 ± 50 Hz vs. high variation = 115 ± 38 Hz, $p = 1.5e-7$, $n = 15$, Fig. 4B1). Next, we assessed temporal coding fidelity using two complementary metrics: VS and correlation index (CI). The VS, which measures synchronicity of spikes to the modulation cycle, indicated robust phase-locking for 200 Hz and 600 Hz modulation frequencies and the VS value significantly decreased with increasing input variation (main effect of variation: $p = 5.8e-14$, 600 Hz**:** no variation = 0.51 ± 0.06 vs. high variation = 0.37 ± 0.03, $p = 7.2e-10$, Fig. 4B2). This is consistent with the reduced temporal precision observed during pure-tone stimulation, indicating poorer encoding of the modulation fine-structure. Similarly, the CI, which quantifies spike time precision across stimulus repetitions (Joris et al., 2006; Kessler et al., 2021), also significantly decreased with higher input variation (main effect of variation: $p = 5.9e-13$, 600 Hz: no variation = 1.53 ± 0.12 vs. high variation = 1.26 ± 0.04, $p = 3e-8$, Fig. 4B3). Together, these measures indicate that increased input variation degrades temporal precision relative to the stimulus cycle

235 and reduces spike time consistency across trials. Concurrently, the entrainment index, quantifying
236 the proportion of interspike intervals within 0.5 – 1.5 times the stimulus period (Joris et al., 1994),
237 significantly increased with input variation at low modulation frequencies (main effect of variation:
238 p =4.7e-6, 200 Hz: no variation = 0.6 ± 0.17 vs. high variation = 0.68 ± 0.1, p = 0.01, Fig. 4B4). At
239 200 Hz, the distributions of the measured and simulated entrainment index were broader than
240 those of the vector strength (Fig 4B2), because in contrast to phase-locking, entrainment is linked
241 to firing rate which was also broadly distributed (Fig 4B1).

242 Next, we investigated how well GBC firing rates tracked the stimulus envelope, reflecting their
243 rate-coding capacity. By calculating the normalized cross-correlation (CorrNorm) between the
244 stimulus envelope and the periodically oscillating firing rate, we quantified the GBC's ability to
245 follow the stimulus envelope. Firing rates tracked envelope modulations at 200 Hz and 600 Hz,
246 and CorrNorm increased significantly with input variation at the 200 Hz modulation frequency,
247 indicating an improved neuronal representation of the stimulus envelope (200 Hz: no variation =
248 0.87 ± 0.02 vs. high variation = 0.93 ± 0.01, p = 2.5e-10, Fig. 4B5). In summary, during SAM
249 stimulation, increased input variation shifts the GBC coding strategy by degrading fine-structure
250 temporal precision (Figs. 1C2, 2C) while simultaneously enhancing envelope representation
251 through firing rate modulation. This suggests that GBC receiving different convergent patterns of
252 AN inputs might be differentially suited to either favor precise temporal representation, requiring
253 highly coincident inputs, or emphasize envelope tracking via firing rate modulation and generally
254 higher firing rates (Rothman and Young, 1996; Joris and Smith, 2008; Koert and Kuenzel, 2021).

255

256 **Impact of input variation is consistent with morphologically plausible input sizes**

257 As demonstrated by our present results, the degree of variation among endbulb inputs can
258 influence GBC coding motifs, potentially shifting the operational focus between temporal precision
259 (i.e., coincidence detection) and firing rate encoding (latency-first mode). As these interpretations

were based on simulated input amplitudes drawn from a gamma distribution, we further evaluated their *in vivo* relevance by testing whether the observed effects can also be verified with the known morphological variability of GBC synaptic inputs. Therefore, we integrated recent morphological data quantifying endbulb size distributions onto mouse GBC (Spirou et al., 2023). Using these estimates allowed us to constrain synaptic input variations within a plausible morphological range. Specifically, we tested two conditions of synaptic input variation corresponding approximately to our previously employed 'medium' ($v \approx 0.4$, '$morph_{MED}$') and 'high' ($v \approx 0.7$, $morph_{HIGH}$) variation conditions.

GBC responses to pure tones under morphologically constrained input variations were consistent with our previous observations. The '$morph_{HIGH}$' condition significantly increased firing rates at 1 kHz and 3.5 kHz stimulation frequencies compared to the '$morph_{MED}$' condition (1 kHz: $morph_{MED}$ = 90 ± 28 Hz vs. $morph_{HIGH}$ = 116 ± 32 Hz, p = 1.2-9, n = 18, Fig. 5A). Concurrently, temporal precision (VS) at 350 Hz and 1 kHz was significantly reduced under high input variation (1 kHz: $morph_{MED}$ = 0.65 ± 0.04 vs $morph_{HIGH}$ = 0.62 ± 0.05, p = 1.9e-5, Fig. 5B). Analysis of onset responses revealed reduced first-spike latencies (1 kHz: $morph_{MED}$ = 4.1 ± 0.14 ms vs. $morph_{HIGH}$ = 3.99 ± 0.17 ms, p = 4.1e-8, Fig. 5C) but increased temporal jitter at the high input variation condition (1 kHz: $morph_{MED}$ = 0.55 ± 0.11 ms vs. $morph_{HIGH}$ = 0.79 ± 0.1, p = 1.3e-12, Fig. 5D), mirroring the pattern observed with gamma-distributed variations (Figs. 1 and 3). These effects were reproduced with the model incorporating morphological input size estimates. These results suggest that the capacity of input variation to shape GBC output is a direct functional consequence of the morphological heterogeneity among synaptic inputs.

Morphologically plausible input variation impacts encoding of amplitude-modulated sounds

Finally, to confirm the impact of realistic input variations on the encoding of amplitude-modulated sounds, we repeated the SAM stimulation experiments using two morphologically constrained input variations. Consistent with the results from gamma-distributed variations (Fig. 4), higher input variations elevated overall firing rates across modulation frequencies (main effect of variation: $p = 2.9e-10$, e.g. 600 Hz: $morph_{MED} = 96 \pm 38$ Hz vs $morph_{HIGH} = 125 \pm 34$ Hz, $p = 7.4e-9$, $n = 19$, Fig. 6A), whereas temporal precision was reduced (VS: main effect of variation: $p = 3.8e-15$, e.g. 600 Hz: $morph_{MED} = 0.46 \pm 0.04$ vs $morph_{HIGH} = 0.37 \pm 0.02$, $p = 8.1e-12$; CI: main effect of variation: $p = 2.5e-18$, e.g. 600 Hz: $morph_{MED} = 1.43 \pm 0.07$ vs $morph_{HIGH} = 1.26 \pm 0.03$, $p = 1.2e-10$, Fig. 6B and C). Rate-coding fidelity (CorrNorm) was enhanced at 200 Hz modulation frequency under high variation (main effect of variation: $p = 3.8e-11$, 200 Hz: medium variation = 0.89 ± 0.01 vs high variation = 0.93 ± 0.01 Hz, $p = 2.9e-17$, Fig. 6D). These findings further support the conclusion that the degree of morphological heterogeneity among GBC endbulb inputs dictates the balance between temporal and rate-coding strategies during the processing of both simple and complex sounds.

Discussion

The heterogeneity of synaptic inputs converging onto neurons is a fundamental aspect of neural circuit design. The strength and variability of these inputs profoundly shape neuronal output and, consequently, determine a neuron's computational role within its circuit. In this study, we investigated how such input strength variation affects GBC which receive multiple, variably sized endbulb inputs from the AN. Our findings demonstrated that the degree of variation among these endbulb inputs critically determines GBC firing characteristics. The present results revealed a functional trade-off: increased input variability enhances overall firing rates and improves the encoding of stimulus amplitude modulations. Simultaneously it degrades temporal precision in representing the stimulus fine-structure and increases onset spike jitter. The modeling results, which extended the experimental observations by testing a wider range of input variations, demonstrated that this functional transition occurs continuously. This suggests that morphological variation in synaptic strength allows GBC to operate along a functional continuum shaped by their respective input configurations.

Limitations and biological context

Endbulb terminals are generally well-spaced across the GBC's somatic surface, likely minimizing the interaction between individual inputs (Nicol and Walmsley, 2002; Spirou et al., 2023). Accordingly, our experimental and modeling approaches assumed a linear summation of statistically independent synaptic inputs. While this approach effectively characterized the core phenomena and revealed a robust effect across individual neurons, additional complexities that are not captured by our current approach might exist. For instance, multiple endbulb inputs originating from the same AN fiber or exhibiting highly correlated activity might functionally act as a single, large input, potentially reducing the effective degree of input variation onto the postsynaptic cells. Additionally, while GBC dendrites are typically short, some endbulb arborizations may synapse onto them (Ostapoff and Morest, 1991; Spirou et al., 2005; Gómez-Nieto and Rubio, 2009). Active dendritic properties could provide slower modulation or alter

integration dynamics in a state-dependent manner, which is not currently accounted for in our model (Häusser and Mel, 2003; Koert and Kuenzel, 2021; Spirou et al., 2023). However, the robust reproduction of key experimental findings using a simple coincidence-counting model suggests that input variation is the most fundamental driver of the observed effects. Future work should investigate how these effects might be altered by somatic and dendritic inhibition and other modulatory factors, which have been shown to impact temporal precision and sound encoding (Kopp-Scheinpflug et al., 2002; Dehmel et al., 2010; Nerlich et al., 2014; Keine and Rübsamen, 2015; Goyer et al., 2016; Keine et al., 2016, 2017).

Species-dependent differences in input convergence

The number of endbulbs converging onto GBC varies across species. Our recordings were performed in Mongolian gerbils, for which detailed anatomical data on input convergence and variation are currently unavailable. However, the observed effects of input variation were consistent across recorded cells, suggesting a mechanism independent of the exact number of endbulbs terminating on a single neuron. Furthermore, the ability of our model to replicate these effects suggests that the underlying mechanism is robust across species-specific differences in input number and variation. By constraining input variations with morphological data from mouse GBC (Spirou et al., 2023), we demonstrated that biologically plausible variations in input sizes are sufficient to induce the observed effects on GBC coding.

The source of this variation is not well understood. In mice, BC inputs were found to originate from different spiral ganglion neuron (SGN) subtypes, each exhibiting differential responses to sound (Wang et al., 2021; Wong et al., 2025). In cats, endbulb inputs onto each individual BC appear to originate predominantly from the same SGN subtype, with endbulbs originating from type Ia SGN typically being larger than those from type Ic SGN (Rouiller et al., 1986; Sento and Ryugo, 1989; Liberman, 1991). If different SGN subtypes systematically provide larger or smaller endbulb inputs in gerbils, this could introduce synaptic heterogeneity that is not explicitly covered by our current

351 approach. However, in mice, SGN inputs onto the same BC exhibit comparable short-term
352 plasticity, and no differences in firing threshold or spontaneous firing rate have been observed in
353 BCs contacted by different proportions of SGN subtypes (Wong et al., 2025). This finding suggests
354 that intrinsic variations in synapse size, potentially independent of SGN subtype, may be a
355 significant factor driving the observed effects.

356 **Functional implications for auditory processing**

357 GBCs provide the primary excitatory input to the MNTB, where their large-diameter axons form
358 the calyx of Held synaptic terminals. The calyx–MNTB synapse functions as a crucial relay (Moore
359 and Caspary, 1983; Wenthold et al., 1987; Wu and Kelly, 1993; Borst and Soria van Hoeve, 2012;
360 Keine and Englitz, 2025), providing well-timed inhibition to several key nuclei in the superior olivary
361 complex (SOC) involved in sound localization (e.g. medial superior olive, MSO; lateral superior
362 olive, LSO) and gap detection (superior paraolivary nucleus, SPN) (Spangler et al., 1985; Sommer
363 et al., 1993; Smith et al., 1998; Srinivasan et al., 2004; Kopp-Scheinpflug et al., 2011).

364 Our findings, together with simulations based on detailed EM reconstructions (Spirou et al., 2023),
365 suggest that the GBC population is not functionally uniform but exhibits considerable diversity
366 driven by AN input variations. GBC receiving endbulb inputs of similar sizes could act as high-
367 fidelity temporal relays, preserving and even enhancing temporal precision essential for binaural
368 computations on a sub-millisecond timescale required for sound localization (Yin and Chan, 1990;
369 Tollin and Yin, 2005; Grothe et al., 2010; Spirou et al., 2023). Conversely, GBC receiving highly
370 variable inputs, characterized by one or two large suprathreshold endbulbs alongside smaller
371 ones, may sacrifice some temporal precision to emphasize a more robust rate code. This
372 enhances their ability to track stimulus envelopes and provides short response latencies, albeit
373 with increased temporal jitter. Indeed, morphological data from mice, combined with computational
374 modeling, suggest that approximately half of the GBC operate in a coincidence detection mode,
375 while the other half show a mixed-mode of operation (Spirou et al., 2023).

376 The implications of this GBC heterogeneity on downstream targets are intriguing. Although MNTB
377 neurons are typically considered a homogenous group of cells, their calyx of Held inputs exhibit
378 considerable structural and functional heterogeneity independent of tonotopic location. For
379 example, MNTB cells contacted by simple calyces tend to exhibit stronger EPSC depression than
380 those contacted by complex calyces (Grande and Wang, 2011; Fekete et al., 2019), indicating
381 potential differences in release probability that may impact their response to sound. It is tempting
382 to speculate that the observed morphological and functional heterogeneity in GBC input variation
383 might be linked to the variations found in their MNTB targets and, ultimately, relate to the specific
384 functional requirements of the auditory nuclei targeted by MNTB neurons. For instance, MNTB
385 inputs to the MSO might require high temporal precision for interaural time difference (ITD) coding,
386 whereas inputs to the LSO might emphasize firing rate encoding for the calculation of interaural
387 level differences (ILDs). Although direct evidence linking GBC input variation to specific calyx
388 subtypes or SOC targets is currently lacking, our results suggest that input variation is essential
389 for functional heterogeneity within these auditory pathways.

390 **Computational mechanisms of synaptic integration and input variation**

391 Computationally, the effects of input variation can be understood by considering how individual
392 inputs interact with the GBC's AP threshold. High input variation, characterized by a few strong
393 inputs, allows a GBC to operate near the AP threshold driven by a small number of coincident or
394 even individual strong inputs (Xu-Friedman and Regehr, 2005a). While this increases overall spike
395 probability and firing rate, it may also result in stimulus-independent or less precisely timed "false-
396 positive" spikes, contributing to an increased temporal jitter. Conversely, configurations with many
397 uniform small inputs require the near-coincident arrival of multiple inputs, thereby enforcing strict
398 coincidence detection and higher temporal fidelity, albeit at the expense of longer response
399 latencies and a reduced overall firing rate (Rothman et al., 1993; Joris et al., 1994; Rothman and
400 Young, 1996; Xu-Friedman and Regehr, 2005b). This principle of integrating strong and weak
401 synaptic inputs to shape neuronal output is a common strategy observed in various brain regions,

402 including the cortex and thalamus (Sherman and Guillery, 1998; Rouiller and Welker, 2000; Groh
403 et al., 2008; Wolff et al., 2021; Govindaiah et al., 2023). Such heterogeneous neuronal populations
404 have been shown to enhance learning of tasks with temporal structure (Perez-Nieves et al., 2021).
405 Our findings place GBC within this broader framework, demonstrating how synaptic input variation
406 tunes synaptic integration to support diverse coding strategies, even at this early stage of sensory
407 processing (Ashida et al., 2019; Spirou et al., 2023). This heterogeneity would ultimately be critical
408 for tailoring neuronal information coding to the various computational demands of downstream
409 auditory circuits.

410

Resource Availability

Lead contact

Requests for further information and resources should be directed and will be fulfilled by Ivan Milenkovic (ivan.milenkovic@uol.de) or Go Ashida (go.ashida@uol.de)

Materials availability

No unique reagents have been generated in this study.

Data and code availability

All numerical data used to generate figures are available at [DOI will be added] under the terms of Creative Commons Attribution 4.0 License (CC BY 4.0).

Acknowledgments

This work was funded by the Deutsche Forschungsgemeinschaft (DFG, German Research Foundation) under Germany's Excellence Strategy – EXC 2177/1 - Project ID 390895286. and intramural funding to CK (Carl von Ossietzky Universität Oldenburg; FP 2024-099)

Author contributions:

CW: Investigation; **GA:** Conceptualization, Methodology, Software, Verification, Formal Analysis, Resources, Data Curation, Writing – Review & Editing; **CK:** Conceptualization, Methodology, Software, Verification, Formal Analysis, Resources, Data Curation, Writing – Original Draft, Writing – Review & Editing, Visualization, Supervision, Funding acquisition; **IM:** Conceptualization, Resources, Writing – Review & Editing, Supervision, Project administration

432 **Declaration of interests**

433 The authors declare no competing interests

434 **STAR Methods**

435 **Experimental Model and Subject Details**

436 **Animals and ethical approval**

437 All experiments were performed at the Physiology Laboratories of the Department of Human
438 Medicine at the University of Oldenburg. Experimental protocols were approved and conducted
439 according to the German Animal Welfare Act (TSchG §4) and European Union Directive
440 2010/63/EU. Mongolian gerbils (*Meriones unguiculatus*) were group-housed under a standard 12h
441 light/dark cycle with unrestricted access to food and water. Experiments were performed on young
442 adult gerbils (postnatal day P20–P25) of both sexes (35 animals, 12 female). All available
443 measures were taken to minimize the number of animals used and alleviate any potential pain or
444 distress.

445 **Method details**

446 *Acute brain slice preparation*

447 Following rapid decapitation, acute parasagittal slices (200 µm thickness) containing the CN were
448 prepared using a vibrating microtome (Leica VT1200 S) equipped with zirconia ceramic blades
449 (EF-INZ10, Cadence Blades). Slicing was performed in ice-cold, low-calcium artificial
450 cerebrospinal fluid (aCSF) containing (in mM): 125 NaCl, 2.5 KCl, 0.1 $CaCl_2$, 3 $MgCl_2$, 1.25
451 NaH_2PO4, 25 $NaHCO_3$, 10 glucose, 3 myo-inositol, 2 sodium pyruvate, and 0.4 ascorbic acid. The
452 aCSF was continuously oxygenated with carbogen gas (5% CO_2 and 95% O_2) and maintained at
453 pH 7.4. Slices were then transferred to a holding chamber containing standard recording solution
454 at near-physiological temperature (36–37°C; identical to the slicing aCSF, except $CaCl_2$ and $MgCl_2$
455 were adjusted to 1.2 mM and 1 mM, respectively), allowed to recover for 30–45 min, and stored

456 thereafter until used for recordings. All solutions were prepared using ultrapure water
457 (0.055 μS/cm).

458 *Electrophysiology*

459 For electrophysiological recordings, slices were placed in a recording chamber continuously
460 perfused with oxygenated aCSF (~1 mL/min) and maintained at physiological temperature
461 (~37°C). Both the recording chamber and perfusion inlet were temperature-controlled using a dual
462 automatic temperature controller (TC-344B, Warner Instruments), and the bath temperature was
463 monitored throughout the experiments. Neurons within the CN were visualized using an upright
464 microscope (Axioskop 2 FS plus, Zeiss) equipped with a water-immersion 63x objective (W Plan-
465 Apochromat 63x/1.0, Cat# 421480-9900-000, Zeiss) and a CCD camera (IR-1000, DAGE-MTI).

466 Recording pipettes were pulled from borosilicate glass (GB-150F-8P, Science Products) to a
467 resistance of 3–5 MΩ when filled with an intracellular solution containing (in mM): 120 K-gluconate,
468 20 KCl, 5 EGTA, 10 HEPES, 0.05 $CaCl_2$, 5 Na_2-phosphocreatine, 4 Mg-ATP, and 0.3 Na-GTP,
469 supplemented with 0.2% biocytin for post-hoc morphological verification. Whole-cell recordings
470 were made using a Multiclamp 700B amplifier (Molecular Devices), digitized at a 100 kHz sampling
471 rate with a Digidata 1440A interface (Molecular Devices) and acquired using pClamp software
472 (RRID:SCR_011323, version 11.2.2, Molecular Devices). In current-clamp mode, the resting
473 membrane potential was held near -60 mV using a small bias current (<140 pA). Series resistance
474 was typically <10 MΩ and was fully compensated via bridge balance. Bridge balance and pipette
475 capacitance neutralization were carefully adjusted and monitored throughout each recording. All
476 experiments were performed at 36–37°C.

477 *Simulating auditory nerve fiber input*

478 The spiking activity of AN fibers was simulated using the 2018 version of the auditory periphery
479 model (Bruce et al., 2018). We used the 'cat' configuration in the model, as AN fiber responses in
480 gerbils share many similarities with those in cats (Versteegh et al., 2011; Huet et al., 2016;

481 Heeringa et al., 2023). Based on observations that GBC primarily receive inputs from high-
482 spontaneous rate (SR) type Ia SGN (Liberman, 1991; Wang et al., 2021; Wong et al., 2025), we
483 set the SR of the model fibers to 70 spikes/s. Refractory periods were fixed at the midpoint of the
484 model's default parameter range, representing typical physiological values (absolute: 0.45 ms,
485 relative: 0.5125 ms).

486 Based on anatomical studies, showing that GBC receive around 5-12 endbulb inputs in mice and
487 around 20 in cats (Spirou et al., 2005, 2023), we simulated the convergence of 10 AN inputs for
488 each target GBC. Because GBC exhibit narrow frequency tuning similar to that of AN fibers
489 (Rhode and Smith, 1986), all converging simulated AN fibers were assumed to share the same
490 characteristic frequency (CF). For pure-tone stimuli, the fibers' CF matched the tone frequency;
491 for amplitude-modulated (AM) sounds, the CF matched the carrier frequency. Sound intensity was
492 set to 70 dB SPL for pure tones and 25 dB SPL for AM sounds.

493

494 *Controlling synaptic input variation*

495 To investigate the impact of heterogeneity among converging inputs, we systematically varied the
496 strength of the 10 simulated AN fibers. Synaptic input variation (*v)* was quantified as the coefficient
497 of variation, defined as the standard deviation (*s)* of the 10 AN input amplitudes divided by their
498 mean (m; v = s/m). For our primary manipulations, sets of 10 AN amplitudes were drawn from a
499 gamma distribution (shape parameter $a = 1/v^2$, scale parameter $b = mv^2$) to create three distinct
500 variation conditions: 'no variation' (v = 0), 'medium variation' (v = 0.4), and 'high variation' (v = 1)
501 (Fig. 1B). These levels were chosen to encompass a broad range of synaptic size heterogeneity,
502 including the range reported from anatomical estimates of GBC inputs (Spirou et al., 2023).
503 Average input strength was varied between cells to result in GBC firing rates of >100 spikes/s
504 during 350 Hz stimulation and kept constant across input variation conditions.

To confirm the biological relevance of our findings, we also implemented synaptic strength distributions based on the morphological data from (Spirou et al., 2023). Two representative GBC input data sets were selected: one (GBC21) previously characterized as fitting the coincidence detection model (CV ≈ 0.33, approximating our 'medium variation', $morph_{MED}$) and another (GBC18L) fitting the mixed-mode integration model (CV ≈ 0.8, approximating our 'high variation', $morph_{HIGH}$). To facilitate direct comparison between these two morphologically derived input variations, we standardized the number of AN inputs to eight for both conditions.

Conductance-clamp implementation

Synaptic conductance traces (G_{syn}) were generated by convolving the simulated AN spike trains with a stereotypical EPSC waveform. This waveform was modeled as an alpha function with a time constant of 0.2 ms, and the EPSC amplitude for each of the 10 inputs was scaled according to the predefined input variation condition. The total G_{syn} represented the linear summation of the conductances from all simulated AN fibers with the average input strength kept constant between input variation conditions.

These pre-calculated G_{syn} waveforms were implemented using a conductance-clamp system, as described previously (Yang et al., 2015). Briefly, the instantaneous membrane potential (V_m) of the recorded GBC was continuously monitored and digitized using a PCIe-6361 data acquisition card (National Instruments) connected via a BNC-2120 interface (National Instruments). This V_m was then fed into a separate computer running mafDC (courtesy of M. A. Xu-Friedman) within Igor Pro (RRID:SCR_000325, version 8, Wavemetrics). The appropriate AMPA receptor-mediated current (I_{syn}) was then calculated in real-time (latency: 15 µs, AMPAR cycle time: 8 µs), according to Ohm's law, assuming a reversal potential (E_{syn}) of 0 mV, and injected back into the GBC via the recording electrode:

$$I_{syn} = G_{syn}(V_m - E_{syn})$$

529 *Post-hoc morphological identification of GBC*

530 To confirm the identity of recorded cells as GBC based on their morphology and location within
531 the CN, slices containing biocytin-filled neurons were processed for morphological analysis
532 following electrophysiological recordings. Immediately after recording, slices were transferred to
533 a culture dish and fixed with 4% paraformaldehyde (PFA) in 1x phosphate-buffered saline (PBS)
534 overnight at 4°C. Following fixation, slices were thoroughly rinsed with 1x PBS (6 × 5 min) followed
535 by 1x PBS containing 0.3% TritonX-100 (PBST, 6 × 5 min). To visualize the biocytin-filled GBC,
536 slices were incubated for 2.5 h at room temperature with Cy5-conjugated streptavidin (5 µg/mL,
537 Cat#016-170-084, Jackson ImmunoResearch) diluted in PBST. Final rinses consisted of PBST (6
538 × 5 min), PBS (2 × 5 min) and ultrapure water (2x5 min).

539 All incubation and rinsing steps were performed on a tilting shaker in the dark. The slices were
540 then mounted on glass slides using Aqua-Poly/Mount mounting medium (Cat#18606,
541 Polysciences, Inc.). Confocal images of recorded neurons were acquired using a Leica SP8
542 confocal scanning microscope equipped with a 10x (0.3 NA, Cat#11506505) dry objective and a
543 63x (1.4 NA, Cat#11506350) oil-immersion objective using a 647 nm excitation wavelength.

544

545 *Globular bushy cell model*

546 Computational simulations of GBC responses were performed using the "adaptive coincidence-
547 counting model" described previously (Ashida et al., 2019). In this model, each incoming spike
548 from a simulated AN fiber evoked a simplified rectangular postsynaptic response (Fig. 2A). The
549 duration (W) of this rectangle remained constant for all inputs, whereas its amplitude (A) was
550 varied across the 10 inputs based on the specified input variation condition described in an earlier
551 section. These individual postsynaptic responses were linearly summed to produce the total
552 integrated input u(t). The model generated an output spike when u(t) exceeded an adaptive

553 threshold $\theta(t)$. Following an output spike, the model entered an absolute refractory period (R)
554 during which no further spikes could be triggered.

555 The adaptive threshold consisted of static and dynamic components: $\theta(t) = \theta_S + \theta_D(t)$. The static
556 component θ_S was fixed at 1, so that postsynaptic response amplitudes (A) were considered
557 normalized to this static input threshold. The dynamic component θ_D changed according to the
558 total input amplitude: $T(d\theta_D/dt) = -\theta_D(t) + S \cdot (u(t))^2$, where T is the time constant and S is the
559 strength of adaptation (Ashida et al., 2019). The quadratic exponent of u(t) was designed to mimic,
560 in a simplified manner, the nonlinear activation of various adaptive mechanisms in BC, such as
561 low-threshold K^+ channels and inhibitory feedback from other CN neurons. This adaptive threshold
562 mechanism allowed the model to reject poorly synchronized inputs, preventing them from reaching
563 the threshold (Fig. 2A). The spike generation mechanism implemented in the GBC model is
564 deterministic and does not produce spike time jitter. To simulate this intrinsic variability, a spike-
565 generation delay $D_{spike} = D_{fix} + D_{rand}$ was added to each output spike timing. The fixed component
566 D_{fix} was set to 0.2 ms, and the random component D_{rand} was drawn from an alpha distribution (Xu-
567 Friedman and Regehr, 2005a) with a time constant of 0.1 ms. This modification was based on the
568 spike latency data from pure-tone stimulation (Fig 3B5 and 3B6) and resulted in a mean increase
569 in response latency of 0.4 ms (SD = 0.14 ms).

570

571 *Model parameters and validation*

572 In addition to the input variation described above, the GBC model used in this study had five free
573 parameters (Table 1). First, a default parameter set was established that generated exemplary
574 responses to pure-tone stimuli resembling those observed in our dynamic-clamp experiments
575 (e.g., PSTHs and raster plots in Fig. 3). To confirm the robustness of the modeling results, we
576 systematically varied the modeling parameter values around the default set (Table 1, right
577 column). Each "model instance", representing a unique parameter combination, was tested with

578 pure-tone stimulation. Only those instances exhibiting GBC-like responses, as defined by the
579 quantitative criteria described below, were adopted for further simulations.

580 The adoption criteria were based on our experimental observations (Figs. 1 and 3). Model
581 instances were required to satisfy the following criteria: (1) spontaneous rate of 10-60 spikes/s;
582 (2) for 350 Hz stimulation: steady-state driven rate >180 spikes/s and vector strength >0.85; (3)
583 for 3500 Hz stimulation: steady-state driven rate of 80-180 spikes/s and onset spike probability
584 >0.95. Furthermore, the PSTH shape near the onset of the 3500 Hz tone was examined to ensure
585 a primary-like-with-notch (PL_N) spiking pattern, characterized by a sharp peak followed by a notch
586 (pause of spiking activity) and a smooth recovery towards the steady-state spiking response (Fig.
587 3A2). Specific criteria for the PL_N response were as follows: (4) the notch appeared within 3 ms
588 after the onset peak; (5) the notch amplitude (minimum rate in PSTH) was below 50% of the
589 steady-state spike rate; (6) a second peak in the PSTH was absent or below 300 spikes/s; (7) the
590 average spike rate at 6-10 ms after the stimulus onset was >90% of the steady-state spike rate;
591 and (8) a second notch was absent or higher than 50% of the steady-state spike rate. The last
592 criterion was used to distinguish PL_N-type PSTHs from chopper-type PSTHs (Ashida et al., 2019).
593 Of the 28,812 model instances tested, 313 (1.1%) met all of these physiological response criteria
594 to be considered 'GBC' and were used in all subsequent simulations.

595

596 **Quantification and statistical analysis**

597 Individual GBC were treated as independent biological samples. Aggregated data are presented
598 as mean ± standard deviation, unless otherwise noted. All comparisons involved within-cell
599 manipulations (i.e., stimulus type and input variation for the same cell) and were analyzed using
600 a multifactorial repeated-measures ANOVA (two-way RM ANOVA). Post-hoc multiple
601 comparisons were corrected using the Bonferroni method (Bonferroni, 1936). A p-value <0.05 was
602 deemed statistically significant for all interpretations. No significant difference was detected

603 between sexes regarding firing rate (p = 0.25) or temporal precision (p = 0.86); therefore, data
604 from both sexes were pooled for further analysis. Sample sizes were determined based on
605 previous similar studies and the typical variance observed for these electrophysiological
606 measures. No statistical methods were used to pre-determine sample sizes prior to data collection.

607 *Electrophysiological data analysis*

608 All data analyses were performed using custom-written scripts in MATLAB (RRID:SCR_001622,
609 Version 2024b, The Mathworks). Action potentials (APs) were detected offline using a voltage
610 threshold crossing criterion of -20 mV. Detected events were visually inspected and curated to
611 exclude potential artifacts. For all subsequent analyses, the time of the AP peak was used as the
612 spike time. Average firing rates were calculated during the period of acoustic stimulation (evoked
613 rate, 150–200 ms duration) or from periods outside the stimulation window (spontaneous rate, 150
614 ms duration). Onset probability was assessed within 1.5 ms of the stimulus-evoked response
615 onset and calculated as the fraction of trials with at least one AP within that time window.
616 Peristimulus time histograms (PSTH) were constructed by binning spike times (bin width = 0.5 ms)
617 across 100–200 identical stimulus repetitions. Phase-locking to periodic stimuli (pure tones or
618 SAM) was quantified with vector strength (VS) (Goldberg and Brown, 1969). To assess spike
619 timing precision independent of the stimulus waveform, the correlation index (CI) was calculated
620 as the normalized peak height of the shuffled autocorrelogram, constructed across identical
621 stimulus repetitions (Joris et al., 2006). For SAM stimuli, the representation of the stimulus
622 envelope in the GBC firing rate was quantified using the normalized cross-correlation (CorrNorm)
623 between the stimulus envelope and the corresponding response PSTH, after correcting for the
624 neuron's response latency (Tolnai et al., 2008; Keine et al., 2016). Note that CorrNorm values
625 range from 0 to 1; unmodulated responses typically yield a CorrNorm value around 0.82, while
626 values >0.9 indicate robust tracking of the stimulus envelope.

627

628 **Figure Legends**

629

630 **Fig. 1: Synaptic input variability increases firing rates at the expense of temporal precision**.
631 **A)** GBC identification based on morphological and electrophysiological features. **A1)** Left: Low-
632 magnification image of cochlear nucleus parasagittal slice containing a biocytin-filled GBC near
633 the AN root (arrow). AVCN: anteroventral cochlear nucleus; PVCN: posteroventral cochlear
634 nucleus; DCN: dorsal cochlear nucleus; AN: auditory nerve. Right: High-magnification image of
635 the GBC shown on the left, displaying its characteristic round soma and a small number of short
636 dendrites. **A2)** Electrophysiological signature of a GBC (top) responding with one or a few APs at
637 the onset of suprathreshold depolarizing current injection (bottom) and voltage sag in response to
638 hyperpolarizing current injection. **B)** Schematic of the experimental paradigm: Acoustic stimuli
639 (top) were processed by an auditory nerve model to generate spike trains for 10 AN fibers (ANF1-
640 10). These spike trains were convolved with the EPSC waveform to generate conductance
641 templates with varying synaptic strengths ranging from 'no variation' (blue) to high variation
642 (orange) and injected into the GBC. Histograms illustrate input variations for the different
643 conditions used. The GBC response (bottom right) was recorded, and the number and timing of
644 the APs (gray triangles) were analyzed. **C1)** Population data (n = 15) of the average GBC firing
645 rate in response to pure-tone stimuli at 350, 1000, and 3500 Hz under three input conditions (blue:
646 no variation, green: medium variation, orange: high variation). The gray triangles indicate the
647 average values for the AN input. Firing rates increased with input variation for 1000 Hz and 3500
648 Hz stimulation. **C2)** Temporal precision quantified as vector strength decreases with input
649 variation, particularly at lower stimulation frequencies. Boxplots show median, IQR with whiskers
650 extending to 1.5 × IQR. Individual cells are represented by gray circles. P-values were calculated
651 using 2-way RM ANOVA with Bonferroni post-hoc tests.

652

Fig. 2: Adaptive coincidence-counting model reproduces experimental data. **A)** Schematic illustration of the GBC model. Top: Example spike trains of four AN fibers highlighting different spike synchrony. Middle: Model responses to the AN fiber inputs with no (blue) and high (orange) input variations. The adaptive threshold changes dynamically according to the recent history of the summed inputs (internal state). GBC model output spikes are generated when the summed inputs exceed the adaptive threshold (blue and orange circles). Note that in the 'high variation' condition spikes can be generated with fewer and less synchronous AN fiber inputs due to the presence of strong individual inputs. **B)** Average firing rates for 313 GBC model instances in response to pure-tone stimuli at 350 Hz, 1000 Hz, and 3500 Hz across input variations. Colored data indicate the input variations used also for our *in vitro* experiments (blue: no variation; green: medium variation; orange: high variation). The model reproduces the experimental trend of higher firing rates for larger input variations at 1000 and 3500 Hz pure-tone stimulation. **C)** Temporal precision quantified as vector strength was slightly reduced with increasing input variation, mirroring the experimental results. Box plots show the range of values from all 313 model instances with thick, medium, and thin boxes indicating 25-75, 10-90, and 0-100 percentiles, respectively.

Fig. 3: Synaptic input variation increases sustained firing rates but reduces onset spike-time precision. **A1)** Peristimulus time histogram (PSTH) of the AN inputs in response to a 3500 Hz pure-tone stimulus. Note the characteristic sharp onset followed by an adapting sustained rate. **A2)** Representative GBC output PSTH in response to the AN input shown in A1 for no variation (blue) and high variation condition (orange). **A3)** Output of the GBC model in response to the same stimulus under no variation (blue) and high variation (orange) conditions, mirroring the experimental data. Insets in A2-A3 show a magnified view of the response onset, highlighting the reduced onset peak under the 'high variation' condition. **B)** Experimental population data (n=17) quantifying GBC response properties for different input variations (blue: no variation, green: medium variation, orange: high variation). **B1)** Raster plot (15 repetitions) of the first spike within 1.5 ms of stimulus onset during 'no variation' (top, blue) and 'high variation' (bottom, orange) conditions. Note the slightly earlier but more variable first spike in the 'high variation' condition. **B2)** Onset spike probability was significantly reduced with input variation, whereas **B3)** sustained firing rates (50-200 ms of the GBC response, and **B4**) spontaneous firing rates increased with input variation. Gray triangles indicate the mean values of the AN input. **B5**) The average first-spike latency decreased with input variation, whereas **B6)** first-spike jitter, defined as the standard deviation of the first-spike latencies, increased with input variation. **C1-C6**). Output of the GBC model quantifying the same parameters as for the experimental data in B1-B6. Colored box plots indicate the input variations used in the *in vitro* experiments. In B) box plots show median, IQR with whiskers extending to 1.5 × IQR. Individual cells are represented by gray circles. P-values were calculated using 2-way RM ANOVA with Bonferroni post-hoc tests. In C), box plots for the modeling data show the range of values from all 313 model instances with thick, medium, and thin boxes indicating 25-75, 10-90, and 0-100 percentiles, respectively.

Fig. 4: Synaptic input variation shapes GBC encoding of amplitude-modulated sounds. A1) Example of simulated AN fiber response to a 200-Hz amplitude-modulated sound (top). The AN firing rate was robustly modulated by the stimulus envelope. Note that the stimulus was aligned with the AN firing rate modulation for display purposes. **A2)** PSTH of representative GBC in response to the AN input shown in A1 under the conditions of 'no variation' (blue) and 'high variation' (orange). Note the broader peaks in the 'high variation' condition. **A3)** GBC model response to the same input variations as shown in A2. The general PSTH shape, including broader peaks in the 'high variation' condition, was well reproduced in the model. **B)** Population data (n=15) quantifying various aspects of the response to amplitude-modulated sounds across three input variations (blue: no variation, green: medium variation, orange: high variation) for modulation frequencies of 200 Hz, 600 Hz and 2000 Hz. For each panel the experimental data are shown on the left and the modeling responses on the right. **B1)** The average firing rates generally increased with input variation across all modulation frequencies. **B2-B3)** Vector strength and correlation index decreased significantly with input variation. **B4-B5)** Entrainment index as well as CorrNorm increased with input variation at low modulation frequencies and remained unchanged at high modulation frequencies. Box plots containing experimental data show median, IQR with whiskers extending to 1.5 × IQR. Individual cells are represented by gray circles. P-values were calculated using 2-way RM ANOVA with Bonferroni post-hoc tests. Box plots for the modeling data show the range of values from all 313 model instances with thick, medium, and thin boxes indicating 25-75, 10-90, and 0-100 percentiles, respectively.

713 **Fig. 5**: **Morphological input variation drives GBC functional heterogeneity**. Population data
714 (n=18) comparing the responses to pure-tone stimulation under two input variation conditions
715 derived from morphological estimates: 'medium variation' (CV ≈ 0.33, green, GBC21) and 'high
716 variation' (CV ≈ 0.8, orange, GBC18L) (Spirou et al., 2023). Histogram illustrates AN fiber strength
717 distribution of eight AN inputs. **A)** Left: High input variation enhanced GBC firing at 1000 Hz and
718 3500 Hz with no effect found at 350 Hz. Right: GBC model responses using the morphological
719 input distribution corroborated the experimental results. **B)** Temporal precision was reduced when
720 GBC receives highly variable inputs. **C)** First-spike latency is slightly reduced at the expense of
721 an increase in first-spike jitter **(D)** with high input variations. Box plots containing experimental
722 data show median, IQR with whiskers extending to 1.5 × IQR. Individual cells are represented by
723 gray circles. P-values were calculated using 2-way RM ANOVA with Bonferroni post-hoc tests.
724 Box plots for the modeling data show the range of values from all 313 model instances with thick,
725 medium, and thin boxes indicating 25-75, 10-90, and 0-100 percentiles, respectively.

Fig. 6: Morphologically constrained input variation alters GBC encoding of amplitude-modulated sounds. Population data (n=19) comparing GBC responses to SAM stimuli at different modulation frequencies under two morphologically constrained input variations: 'medium variation' (CV ≈ 0.33, green, GBC21) and 'high variation' (CV ≈ 0.8, orange, GBC18L) (Spirou et al., 2023). High input variations enhanced firing rates **(A)**, decreased vector strength **(B)** and correlation index **(C)**, and improved representation of the stimulus envelope (CorrNorm, **D**) in both the experimental and the model data. Box plots containing experimental data show median, IQR with whiskers extending to 1.5 × IQR. Individual cells are represented by gray circles. P-values were calculated using 2-way RM ANOVA with Bonferroni post-hoc tests. Box plots for the modeling data show the range of values from all 313 model instances with thick, medium, and thin boxes indicating 25-75, 10-90, and 0-100 percentiles, respectively.

Tables

Table 1: Model parameters. The total number of parameter combinations was 12×7×7×7×7 = 28,812. The default parameter values were used for Figs. 3A3, 3C1, 4A3.

Parameter	Default value	Ranges tested
(mean) Input amplitude *A*	0.38	0.28 − 0.50 (step 0.02)
Input duration (ms) *W*	0.6	0.2 − 1.4 (step 0.2)
Refractory period (ms) *R*	1.5	0.8 − 2.0 (step 0.2)
Adaptation strength *S*	0.8	0.4 − 1.6 (step 0.2)
Adaptation time constant (ms) *T*	0.7	0.3 − 2.1 (step 0.3)

Table 2: Summary of statistical analysis for gamma-distributed input variations

			Variation				
		Stimulus	**no**	**medium**	**high**	**p-value RM ANOVA**	**post-hoc comparisons**
Figure 1 (n=15)	**Firing Rate (Hz)**	**350 Hz**	245 ± 52	239 ± 52	228 ± 39	variation: p=4.6e-5	no vs medium: p=0.1 no vs high: p=0.01 medium vs. high: p=0.05
		1000 Hz	132 ± 48	139 ± 46	171 ± 34		no vs medium: p=0.03 no vs high: p=7.9e-6 medium vs. high: p=6.6e-6
		3500 Hz	119 ± 47	130 ± 48	170 ± 33		no vs medium: p=5.5e-5 no vs high: p=8.9e-7 medium vs. high: p=1.4e-5
	Vector Strength	**350 Hz**	0.86 ± 0.02	0.85 ± 0.01	0.81 ± 0.01	variation: p=3.7e-6	no vs medium: p=0.001 no vs high: p=3.3e-8 medium vs. high: p=4.3e-8
		1000 Hz	0.61 ± 0.08	0.59 ± 0.09	0.57 ± 0.06		no vs medium: p=0.43 no vs high: p=0.005 medium vs. high: p=0.29
		3500 Hz	0.06 ± 0.03	0.05 ± 0.03	0.05 ± 0.02		no vs medium: p=0.57 no vs high: p>0.99 medium vs. high: p>0.99
Figure 3 (n=15)	**Onset probability**	**3500 Hz**	0.97 ± 0.02	0.96 ± 0.02	0.94 ± 0.02	p=3.5e-6	no vs medium: p=0.42 no vs high: p=7.3e-5 medium vs. high: p=0.0004
	Sustained firing rate (Hz)	**3500 Hz**	71.7 ± 26.8	86.6 ± 29.7	130.8 ± 28.2	p=8.7e-16	no vs medium: p=5.8e-5 no vs high: p=3.2e-11 medium vs. high: p=2.7e-12
	Spontaneous firing rate (Hz)	**3500 Hz**	24.83 ± 14.31	34.82 ± 17.8	64.96 ± 14.64	p=2.4e-17	no vs medium: p=0.0009 no vs high: p=4.9e-11 medium vs. high: p=1.8e-9
	First-spike latency (ms)	**3500 Hz**	3 ± 0.14	2.95 ± 0.12	2.92 ± 0.15	p=0.001	no vs medium: p=0.009 no vs high: p=0.007 medium vs. high: p=0.21
	First-spike jitter (ms)	**3500 Hz**	0.42 ± 0.12	0.52 ± 0.17	0.63 ± 0.21	p=5.84e-6	no vs medium: p=0.001 no vs high: p=7.4e-5 medium vs. high: p=3e-4
Figure 4 (n=15)	**Firing Rate (Hz)**	**200 Hz**	130 ± 36	131 ± 33	145 ± 23	variation: p=3e-10	no vs medium: p>0.99 no vs high: p=0.01 medium vs. high: p=0.002
		600 Hz	67 ± 50	77 ± 50	115 ± 38		no vs medium: p=3e-4 no vs high: p=1.47e-7 medium vs. high: p=3.5e-6
		2000 Hz	65 ± 50	71 ± 46	111 ± 43		no vs medium: p=0.12 no vs high: p=7.8e-9 medium vs. high: p=1.4e-9
	Vector Strength	**200 Hz**	0.84 ± 0.03	0.83 ± 0.02	0.76 ± 0.01	variation: p=5.7e-14	no vs medium: p=0.006 no vs high: p=9.3e-10 medium vs. high: p=1.6e-12
		600 Hz	0.51 ± 0.06	0.48 ± 0.05	0.37 ± 0.03		no vs medium: p=2.2e-6 no vs high: p=7.2e-10 medium vs. high: p=9.6e-10
		2000 Hz	0.01 ± 0.01	0.01 ± 0.01	0.01 ± 0		no vs medium: p=0.84 no vs high: p>0.99

							medium vs. high: p=0.1
	Correlation Index	**200 Hz**	3.06 ± 0.19	2.93 ± 0.1	2.39 ± 0.06	variation: p=5.9e-13	no vs medium: p=4e-4 no vs high: p=3.7e-10 medium vs. high: p=1.3e-12
		600 Hz	1.53 ± 0.12	1.46 ± 0.1	1.26 ± 0.04		no vs medium: p=6.2e-6 no vs high: p=3e-8 medium vs. high: p=2.6e-8
		2000 Hz	1.01 ± 0.02	1.01 ± 0.02	1 ± 0.01		no vs medium: p>0.99 no vs high: p=0.5 medium vs. high: p=0.06
	Entrainment Index	**200 Hz**	0.6 ± 0.17	0.62 ± 0.17	0.68 ± 0.1	variation: p=4.7e-6	no vs medium: p=0.87 no vs high: p=0.01 medium vs. high: p=0.04
		600 Hz	0.01 ± 0.01	0.01 ± 0.03	0.04 ± 0.05		no vs medium: p=0.36 no vs high: p=0.005 medium vs. high: p=0.001
		2000 Hz	0 ± 0	0 ± 0	0 ± 0		no vs medium: p=0.44 no vs high: p=0.64 medium vs. high: p>0.99
	CorrNorm	**200 Hz**	0.87 ± 0.02	0.88 ± 0.01	0.93 ± 0.01	variation: p=1.8e-10	no vs medium: p=0.004 no vs high: p=2.5e-10 medium vs. high: p=6.3e-11
		600 Hz	0.99 ± 0.01	0.99 ± 0	0.98 ± 0.01		no vs medium: p=0.027 no vs high: p=0.5 medium vs. high: p=0.003
		2000 Hz	0.82 ± 0.01	0.82 ± 0.01	0.82 ± 0		no vs medium: p>0.99 no vs high: p=0.42 medium vs. high: p=0.26

Table 3: Summary of statistical analysis for morphologically-derived input variations

		Stimulus	**morph$_{MED}$**	**morph$_{HIGH}$**		**post-hoc comparison (morph$_{MED}$ vs morph$_{HIGH}$)**
Figure 5 (n=18)	**Firing Rate (Hz)**	**350 Hz**	149 ± 40	155 ± 31	p=4.6e-11	p=0.1
		1000 Hz	90 ± 28	116 ± 32		p=1.2e-9
		3500 Hz	87 ± 28	119 ± 30		p=3.5e-11
	Vector Strength	**350 Hz**	0.86 ± 0.01	0.82 ± 0.01	p=5.9e9	p=4.1e-11
		1000 Hz	0.65 ± 0.04	0.62 ± 0.05		p=1.9e-5
		3500 Hz	0.02 ± 0.01	0.02 ± 0.01		p=0.38
	First-spike latency (ms)	**350 Hz**	4.67 ± 0.17	4.57 ± 0.14	p=1.2e-6	p=0.0015
		1000 Hz	4.09 ± 0.14	3.99 ± 0.17		p=4.1e-8
		3500 Hz	3.05 ± 0.09	3.04 ± 0.12		p=0.51
	First-spike jitter (ms)	**350 Hz**	0.46 ± 0.2	0.68 ± 0.14	p=7.1e-12	p=2e-4
		1000 Hz	0.55 ± 0.11	0.79 ± 0.11		p=1.3e-12
		3500 Hz	0.34 ± 0.03	0.45 ± 0.08		p=3e-5
Figure 6 (n=19)	**Firing Rate (Hz)**	**200 Hz**	134 ± 30	142 ± 27	p=2.9e-10	p=2e-5
		600 Hz	96 ± 38	125 ± 34		p=7.4e-9
		2000 Hz	89 ± 36	125 ± 31		p=6.2e-11
	Vector Strength	**200 Hz**	0.81 ± 0.02	0.75 ± 0.02	p=3.8e-15	p=2e-17
		600 Hz	0.46 ± 0.04	0.37 ± 0.02		p=8.1e-12
		2000 Hz	0.01 ± 0.01	0.01 ± 0		p=0.07
	Correlation index	**200 Hz**	2.78 ± 0.11	2.33 ± 0.1	p=2.5e-18	p=3.7e-19
		600 Hz	1.43 ± 0.07	1.26 ± 0.03		p=1.2e-10
		2000 Hz	1 ± 0.01	1 ± 0		p=0.19
	CorrNorm	**200 Hz**	0.89 ± 0.01	0.93 ± 0.01	p=3.8e-11	p=2.9e-17
		600 Hz	0.99 ± 0.01	0.98 ± 0		p=0.002
		2000 Hz	0.81 ± 0.01	0.82 ± 0.01		p=0.04

References

Ashida G, Heinermann HT, Kretzberg J (2019) Neuronal population model of globular bushy cells covering unit-to-unit variability. PLoS Comput Biol 15:e1007563.

Blackburn CC, Sachs MB (1989) Classification of unit types in the anteroventral cochlear nucleus: PST histograms and regularity analysis. J Neurophysiol 62:1303–1329.

Bonferroni CE (1936) Teoria statistica delle classi e calcolo delle probabilità. Pubblicazioni del R Istituto Superiore di Scienze Economiche e Commerciali di Firenze 8:3–62.

Borst JGG, Soria van Hoeve J (2012) The calyx of Held synapse: from model synapse to auditory relay. Annu Rev Physiol 74:199–224.

Britt R, Starr A (1976) Synaptic events and discharge patterns of cochlear nucleus cells. I. Steady-frequency tone bursts. J Neurophysiol 39:162–178.

Bruce IC, Erfani Y, Zilany MSA (2018) A phenomenological model of the synapse between the inner hair cell and auditory nerve: Implications of limited neurotransmitter release sites. Hear Res 360:40–54.

Calkins DJ, Schein SJ, Tsukamoto Y, Sterling P (1994) M and L cones in macaque fovea connect to midget ganglion cells by different numbers of excitatory synapses. Nature 371:70–72.

Cant NB, Morest DK (1979) Organization of the neurons in the anterior division of the anteroventral cochlear nucleus of the cat. Light-microscopic observations. Neuroscience 4:1909–1923.

Cao X-J, Oertel D (2010) Auditory nerve fibers excite targets through synapses that vary in convergence, strength, and short-term plasticity. J Neurophysiol 104:2308–2320.

Dehmel S, Kopp-Scheinpflug C, Weick M, Dörrscheidt GJGJ, Rübsamen R (2010) Transmission of phase-coupling accuracy from the auditory nerve to spherical bushy cells in the Mongolian gerbil. Hear Res 268:234–249.

Doucet JR, Ryugo DK (2006) Structural and functional classes of multipolar cells in the ventral cochlear nucleus. Anat Rec A Discov Mol Cell Evol Biol 288:331–344.

Drullman R, Festen JM, Houtgast T (1996) Effect of temporal modulation reduction on spectral contrasts in speech. J Acoust Soc Am 99:2358–2364.

Englitz B, Tolnai S, Typlt M, Jost J, Rübsamen R (2009) Reliability of synaptic transmission at the synapses of held in vivo under acoustic stimulation. PLoS One 4:e7014.

Fekete A, Nakamura Y, Yang Y-M, Herlitze S, Mark MD, DiGregorio DA, Wang L-Y (2019) Underpinning heterogeneity in synaptic transmission by presynaptic ensembles of distinct morphological modules. Nat Commun 10:826.

Fukui I, Ohmori H (2004) Tonotopic gradients of membrane and synaptic properties for neurons of the chicken nucleus magnocellularis. J Neurosci 24:7514–7523.

Goldberg JM, Brown PB (1969) Response of binaural neurons of dog superior olivary complex to dichotic tonal stimuli: some physiological mechanisms of sound localization. J Neurophysiol 32:613–636.

Gómez-Nieto R, Rubio ME (2009) A bushy cell network in the rat ventral cochlear nucleus. J Comp Neurol 516:241–263.

Govindaiah G, Fox MA, Guido W (2023) Pattern of driver-like input onto neurons of the mouse ventral lateral geniculate nucleus. eNeuro 10:ENEURO.0386-22.2022.

Goyer D, Kurth S, Gillet C, Keine C, Rübsamen R, Kuenzel T (2016) Slow cholinergic modulation of spike probability in ultra-fast time-coding sensory neurons. eNeuro 3 Available at: http://eneuro.org/cgi/doi/10.1523/ENEURO.0186-16.2016.

Grande G, Wang L-Y (2011) Morphological and functional continuum underlying heterogeneity in the spiking fidelity at the calyx of Held synapse in vitro. J Neurosci 31:13386–13399.

Groh A, de Kock CPJ, Wimmer VC, Sakmann B, Kuner T (2008) Driver or coincidence detector: modal switch of a corticothalamic giant synapse controlled by spontaneous activity and short-term depression. J Neurosci 28:9652–9663.

Grothe B, Pecka M, McAlpine D (2010) Mechanisms of sound localization in mammals. Physiol Rev 90:983–1012.

Häusser M, Mel B (2003) Dendrites: bug or feature? Curr Opin Neurobiol 13:372–383.

Heeringa AN (2024) Single-unit data for sensory neuroscience: Responses from the auditory nerve of young-adult and aging gerbils. Sci Data 11:1–13.

Heeringa AN, Teske F, Ashida G, Köppl C (2023) Cochlear aging disrupts the correlation between spontaneous rate and sound-level coding in auditory nerve fibers. J Neurophysiol 130:736–750.

Heeringa AN, Zhang L, Ashida G, Beutelmann R, Steenken F, Köppl C (2020) Temporal Coding of Single Auditory Nerve Fibers Is Not Degraded in Aging Gerbils. J Neurosci 40:343–354.

Huang CG, Chacron MJ (2016) Optimized parallel coding of second-order stimulus features by heterogeneous neural populations. J Neurosci 36:9859–9872.

Huet A, Batrel C, Tang Y, Desmadryl G, Wang J, Puel J-L, Bourien J (2016) Sound coding in the auditory nerve of gerbils. Hear Res 338:32–39.

Jacoby RA, Wiechmann AF, Amara SG, Leighton BH, Marshak DW (2000) Diffuse bipolar cells provide input to OFF parasol ganglion cells in the macaque retina. J Comp Neurol 416:6–18.

Johnson DH (1980) The relationship between spike rate and synchrony in responses of auditory-nerve fibers to single tones. J Acoust Soc Am 68:1115–1122.

Joris PX, Carney LH, Smith PH, Yin TCT (1994) Enhancement of neural synchronization in the anteroventral cochlear nucleus. I. Responses to tones at the characteristic frequency. J Neurophysiol 71:1022–1036.

Joris PX, Louage DH, Cardoen L, van der Heijden M (2006) Correlation index: a new metric to quantify temporal coding. Hear Res 216–217:19–30.

Joris PX, Schreiner CE, Rees A (2004) Neural processing of amplitude-modulated sounds. Physiol Rev 84:541–577.

Joris PX, Smith PH (2008) The volley theory and the spherical cell puzzle. Neuroscience 154:65–76.

Joris PX, Yin TCT (1992) Responses to amplitude-modulated tones in the auditory nerve of the cat. J Acoust Soc Am 91:215–232.

Keine C, Englitz B (2025) Cellular and synaptic specializations for sub-millisecond precision in the mammalian auditory brainstem. Front Cell Neurosci 19:1568506.

Keine C, Rübsamen R (2015) Inhibition shapes acoustic responsiveness in spherical bushy cells. J Neurosci 35:8579–8592.

Keine C, Rübsamen R, Englitz B (2016) Inhibition in the auditory brainstem enhances signal representation and regulates gain in complex acoustic environments. Elife 5:19295.

Keine C, Rübsamen R, Englitz B (2017) Signal integration at spherical bushy cells enhances representation of temporal structure but limits its range. Elife 6:29639.

Kessler D, Carr CE, Kretzberg J, Ashida G (2021) Theoretical relationship between two measures of spike synchrony: Correlation index and vector strength. Front Neurosci 15:761826.

Koert E, Kuenzel T (2021) Small dendritic synapses enhance temporal coding in a model of cochlear nucleus bushy cells. J Neurophysiol 125:915–937.

Kolb H, Marshak D (2003) The midget pathways of the primate retina. Doc Ophthalmol 106:67–81.

Köppl C (1994) Auditory nerve terminals in the cochlear nucleus magnocellularis: differences between low and high frequencies. J Comp Neurol 339:438–446.

Kopp-Scheinpflug C, Dehmel S, Dörrscheidt GJ, Rübsamen R (2002) Interaction of excitation and inhibition in anteroventral cochlear nucleus neurons that receive large endbulb synaptic endings. J Neurosci 22:11004–11018.

Kopp-Scheinpflug C, Tozer AJB, Robinson SW, Tempel BL, Hennig MH, Forsythe ID (2011) The sound of silence: ionic mechanisms encoding sound termination. Neuron 71:911–925.

Kreeger LJ, Honnuraiah S, Maeker S, Shea S, Fishell G, Goodrich L (2025) An anatomical and physiological basis for flexible coincidence detection in the auditory system. Elife 13 Available at: https://elifesciences.org/reviewed-preprints/100492.

Liberman MC (1991) Central projections of auditory-nerve fibers of differing spontaneous rate. I. Anteroventral cochlear nucleus. J Comp Neurol 313:240–258.

McGinley MJ, Liberman MC, Bal R, Oertel D (2012) Generating synchrony from the asynchronous: compensation for cochlear traveling wave delays by the dendrites of individual brainstem neurons. J Neurosci 32:9301–9311.

Moore MJ, Caspary DM (1983) Strychnine blocks binaural inhibition in lateral superior olivary neurons. J Neurosci 3:237–242.

Nagayama S, Takahashi YK, Yoshihara Y, Mori K (2004) Mitral and tufted cells differ in the decoding manner of odor maps in the rat olfactory bulb. J Neurophysiol 91:2532–2540.

Nerlich J, Kuenzel T, Keine C, Korenic A, Rübsamen R, Milenkovic I (2014) Dynamic fidelity control to the central auditory system: synergistic glycine/GABAergic inhibition in the cochlear nucleus. J Neurosci 34:11604–11620.

Nicol MJ, Walmsley B (2002) Ultrastructural basis of synaptic transmission between endbulbs of Held and bushy cells in the rat cochlear nucleus. J Physiol 539:713–723.

Oertel D (1999) The role of timing in the brain stem auditory nuclei of vertebrates. Annu Rev Physiol 61:497–519.

Oline SN, Ashida G, Burger RM (2016) Tonotopic optimization for temporal processing in the cochlear nucleus. J Neurosci 36: 8500–8515.

Osen KK (1969) Cytoarchitecture of the cochlear nuclei in the cat. J Comp Neurol 136:453–484.

Ostapoff EM, Morest DK (1991) Synaptic organization of globular bushy cells in the ventral cochlear nucleus of the cat: a quantitative study. J Comp Neurol 314:598–613.

Palmer a. R, Russell IJ (1986) Phase-locking in the cochlear nerve of the guinea-pig and its relation to the receptor potential of inner hair-cells. Hear Res 24:1–15.

Palmer AR, Winter IM, Darwin CJ (1986) The representation of steady-state vowel sounds in the temporal discharge patterns of the guinea pig cochlear nerve and primarylike cochlear nucleus neurons. J Acoust Soc Am 79:100–113.

Perez-Nieves N, Leung VCH, Dragotti PL, Goodman DFM (2021) Neural heterogeneity promotes robust learning. Nat Commun 12:5791.

Rhode WS, Greenberg S (1994) Encoding of amplitude modulation in the cochlear nucleus of the cat. J Neurophysiol 71:1797–1825.

Rhode WS, Smith PH (1986) Encoding timing and intensity in the ventral cochlear nucleus of the cat. J Neurophysiol 56:261–286.

Ritz LA, Brownell WE (1982) Single unit analysis of the posteroventral cochlear nucleus of the decerebrate cat. Neuroscience 7:1995–2010.

Rothman JS, Young ED, Manis PB (1993) Convergence of auditory nerve fibers onto bushy cells in the ventral cochlear nucleus: implications of a computational model. J Neurophysiol 70:2562–2583.

Rothman JSS, Young EDD (1996) Enhancement of neural synchronization in computational models of ventral cochlear nucleus bushy cells. Aud Neurosci 2:47–62.

Rouiller EM, Cronin-Schreiber R, Fekete DM, Ryugo DK (1986) The central projections of intracellularly labeled auditory nerve fibers in cats: an analysis of terminal morphology. J Comp Neurol 249:261–278.

Rouiller EM, Welker E (2000) A comparative analysis of the morphology of corticothalamic projections in mammals. Brain Res Bull 53:727–741.

Schneggenburger R, Forsythe ID (2006) The calyx of Held. Cell Tissue Res 326:311–337.

Sento S, Ryugo DK (1989) Endbulbs of held and spherical bushy cells in cats: morphological correlates with physiological properties. J Comp Neurol 280:553–562.

Sherman SM, Guillery RW (1998) On the actions that one nerve cell can have on another: distinguishing “drivers” from “modulators.” Proc Natl Acad Sci U S A 95:7121–7126.

Smith PH, Joris PX, Yin TCT, J.oris PX (1998) Anatomy and physiology of principal cells of the medial nucleus of the trapezoid body (MNTB) of the cat. J Neurophysiol 79:3127–3142.

Smith PH, Rhode WS (1987) Characterization of HRP-labeled globular bushy cells in the cat anteroventral cochlear nucleus. J Comp Neurol 266:360–375.

Smith RL, Brachman ML (1980) Response modulation of auditory-nerve fibers by AM stimuli: effects of average intensity. Hear Res 2:123–133.

Sommer I, Lingenhöhl K, Friauf E (1993) Principal cells of the rat medial nucleus of the trapezoid body: an intracellular in vivo study of their physiology and morphology. Exp Brain Res:223–239.

Spangler KM, Warr WB, Henkel CK (1985) The projections of principal cells of the medial nucleus of the trapezoid body in the cat. J Comp Neurol 238:249–262.

Spirou GA, Brownell WE, Zidanic M (1990) Recordings from cat trapezoid body and HRP labeling of globular bushy cell axons. J Neurophysiol 63:1169–1190.

Spirou GA, Kersting MG, Carr S, Razzaq B, Alves-Pinto CY, Dawson M, Ellisman MH, Manis PB (2023) High-resolution volumetric imaging constrains compartmental models to explore synaptic integration and temporal processing by cochlear nucleus globular bushy cells. Elife 12:1–44.

Spirou GA, Rager J, Manis PB (2005) Convergence of auditory-nerve fiber projections onto globular bushy cells. Neuroscience 136:843–863.

Srinivasan G, Friauf E, Löhrke S (2004) Functional glutamatergic and glycinergic inputs to several superior olivary nuclei of the rat revealed by optical imaging. Neuroscience 128:617–634.

Tollin DJ, Yin TCT (2005) Interaural phase and level difference sensitivity in low-frequency neurons in the lateral superior olive. J Neurosci 25:10648–10657.

Tolnai S, Englitz B, Kopp-Scheinpflug C, Dehmel S, Jost J, Rübsamen R (2008) Dynamic coupling of excitatory and inhibitory responses in the medial nucleus of the trapezoid body. Eur J Neurosci 27:3191–3204.

Van Tasell DJ, Soli SD, Kirby VM, Widin GP (1987) Speech waveform envelope cues for consonant recognition. J Acoust Soc Am 82:1152–1161.

Versteegh CPC, Meenderink SWF, van der Heijden M (2011) Response characteristics in the apex of the gerbil cochlea studied through auditory nerve recordings. J Assoc Res Otolaryngol 12:301–316.

von Gersdorff H, Borst JGG (2002) Short-term plasticity at the calyx of Held. Nat Rev Neurosci 3:53–64.

Wang M, Zhang C, Lin S, Wang Y, Seicol BJ, Ariss RW, Xie R (2021) Biased auditory nerve central synaptopathy is associated with age-related hearing loss. J Physiol 599:1833–1854.

Wang X, Sachs MB (1994) Neural encoding of single-formant stimuli in the cat. II. Responses of anteroventral cochlear nucleus units. J Neurophysiol 71:59–78.

Wei L, Karino S, Verschooten E, Joris PX (2017) Enhancement of phase-locking in rodents. I. An axonal recording study in gerbil. J Neurophysiol 118:2009–2023.

Wei L, Verschooten E, Joris PX (2023) Enhancement of phase-locking in rodents. II. An axonal recording study in chinchilla. J Neurophysiol 130:751–767.

Wenthold RJ, Huie D, Altschuler R a., Reeks K a. (1987) Glycine immunoreactivity localized in the cochlear nucleus and superior olivary complex. Neuroscience 22:897–912.

Wolff M, Morceau S, Folkard R, Martin-Cortecero J, Groh A (2021) A thalamic bridge from sensory perception to cognition. Neurosci Biobehav Rev 120:222–235.

Wong NF, Brongo SE, Forero EA, Sun S, Cook CJ, Lauer AM, Müller U, Xu-Friedman MA (2025) Convergence of type 1 spiral ganglion neuron subtypes onto principal neurons of the anteroventral cochlear nucleus. J Neurosci 45:e1507242024.

Wu SH, Kelly JB (1993) Response of neurons in the lateral superior olive and medial nucleus of the trapezoid body to repetitive stimulation: Intracellular and extracellular recordings from mouse brain slice. Hear Res 68:189–201.

Xie R, Manis PB (2017) Radiate and planar multipolar neurons of the mouse anteroventral cochlear nucleus: Intrinsic excitability and characterization of their auditory nerve input. Front Neural Circuits 11:77.

Xu-Friedman MA, Regehr WG (2005a) Dynamic-clamp analysis of the effects of convergence on spike timing. II. Few synaptic inputs. J Neurophysiol 94:2526–2534.

Xu-Friedman MA, Regehr WG (2005b) Dynamic-clamp analysis of the effects of convergence on spike timing. I. Many synaptic inputs. J Neurophysiol 94:2512–2525.

Yang Y, Adowski T, Ramamurthy B, Neef A, Xu-Friedman MA (2015) High-speed dynamic-clamp interface. J Neurophysiol 113:2713–2720.

Yin TCT, Chan JCK (1990) Interaural time sensitivity in medial superior olive of cat. J Neurophysiol 64:465–488.

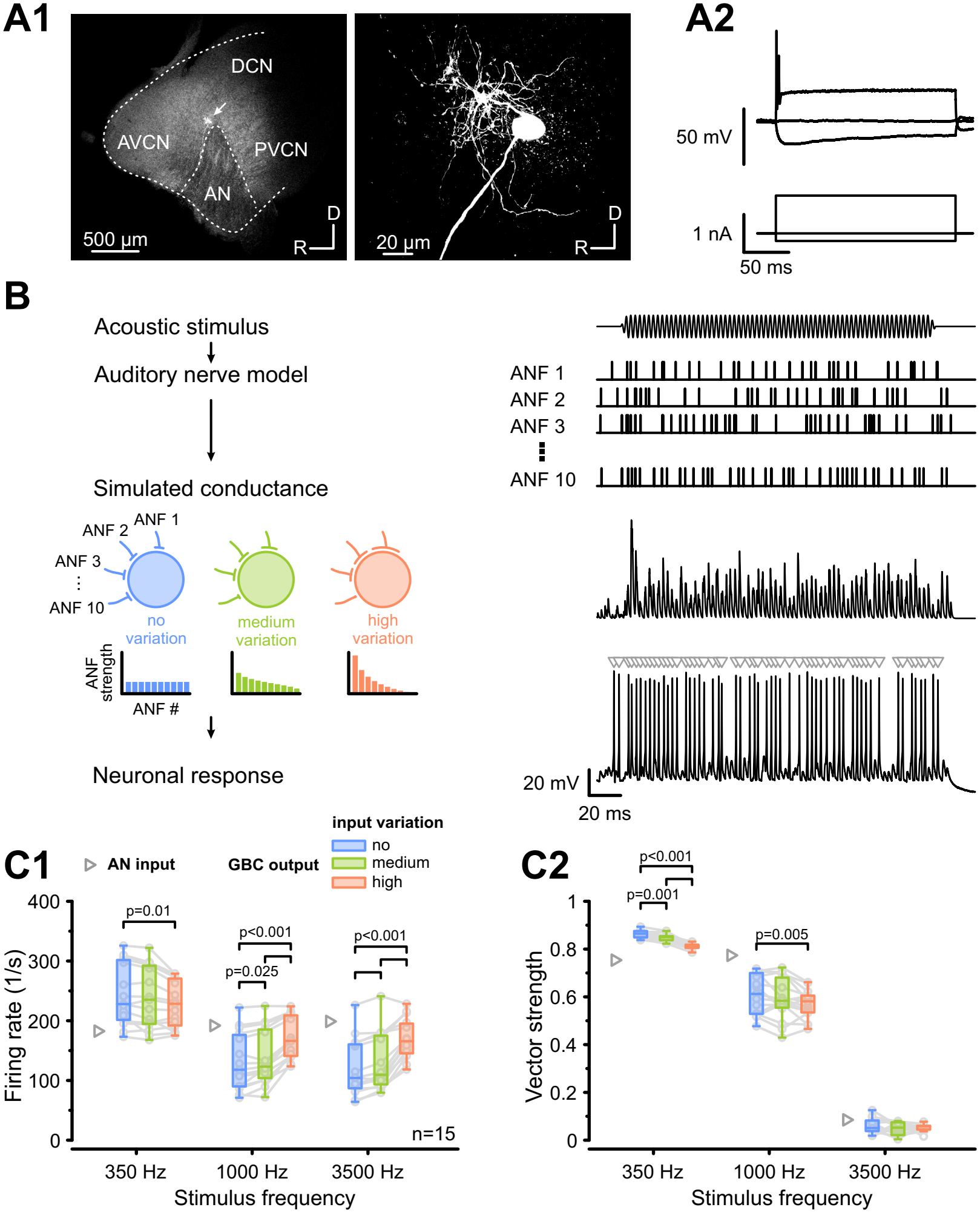
A1
DCN
AVCN
PVCN
AN
500 µm
D
R
20 µm
A2
50 mV
1 nA
50 ms
B
Acoustic stimulus
Auditory nerve model
Simulated conductance
ANF 1
ANF 2
ANF 3
ANF 10
no variation
medium variation
high variation
ANF strength
ANF #
Neuronal response
20 mV
20 ms
C1
AN input
GBC output
input variation
no
medium
high
p=0.01
p<0.001
p=0.025
p<0.001
n=15
Firing rate (1/s)
350 Hz
1000 Hz
3500 Hz
Stimulus frequency
C2
p<0.001
p=0.001
p=0.005
Vector strength
350 Hz
1000 Hz
3500 Hz
Stimulus frequency

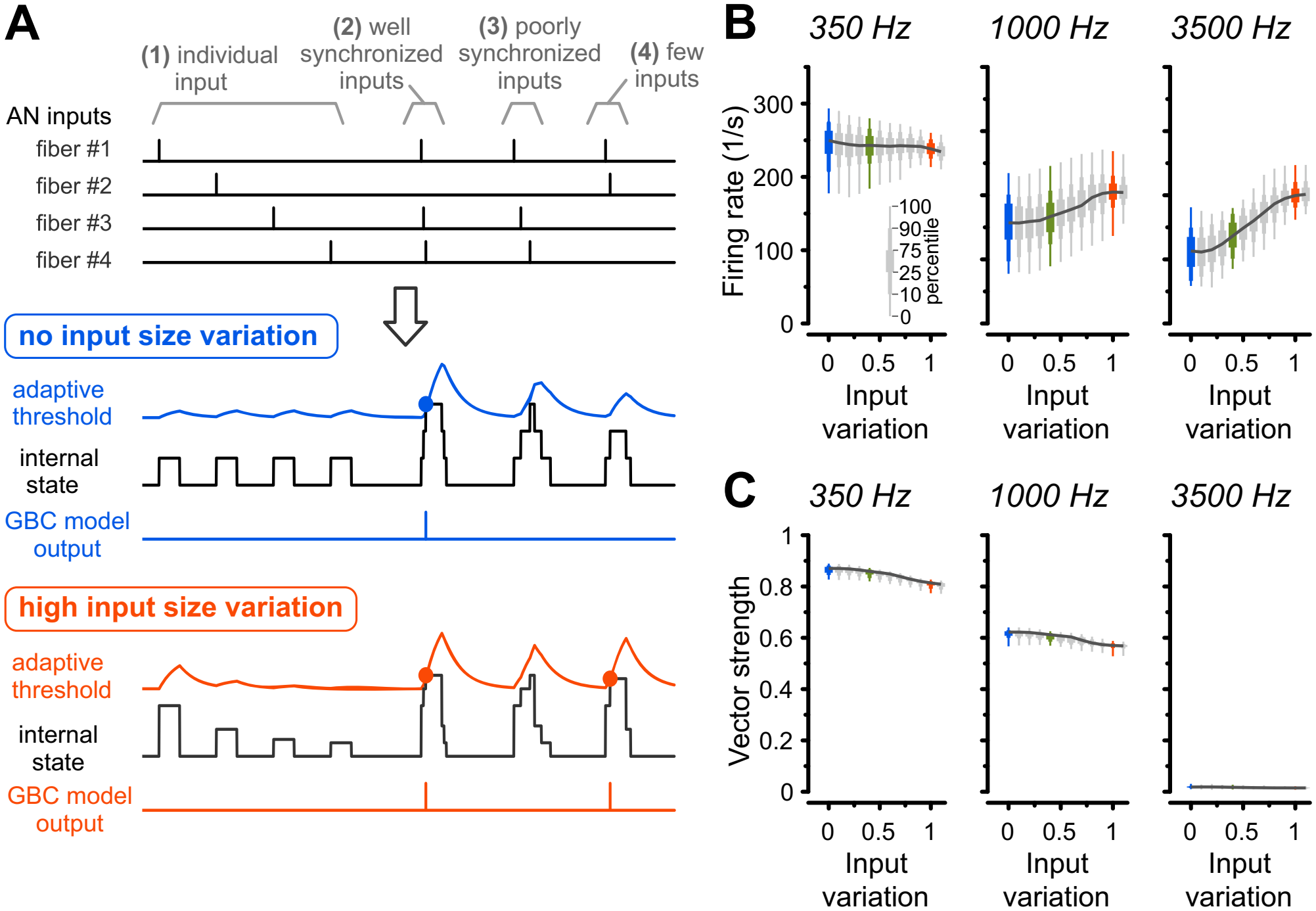
A
(1) individual input
(2) well synchronized inputs
(3) poorly synchronized inputs
(4) few inputs
AN inputs
fiber #1
fiber #2
fiber #3
fiber #4
no input size variation
adaptive threshold
internal state
GBC model output
high input size variation
adaptive threshold
internal state
GBC model output
B
350 Hz
1000 Hz
3500 Hz
Firing rate (1/s)
300
200
100
0
100
90
75
25
10
0
percentile
0
0.5
1
Input variation
C
350 Hz
1000 Hz
3500 Hz
Vector strength
1
0.8
0.6
0.4
0.2
0
0
0.5
1
Input variation

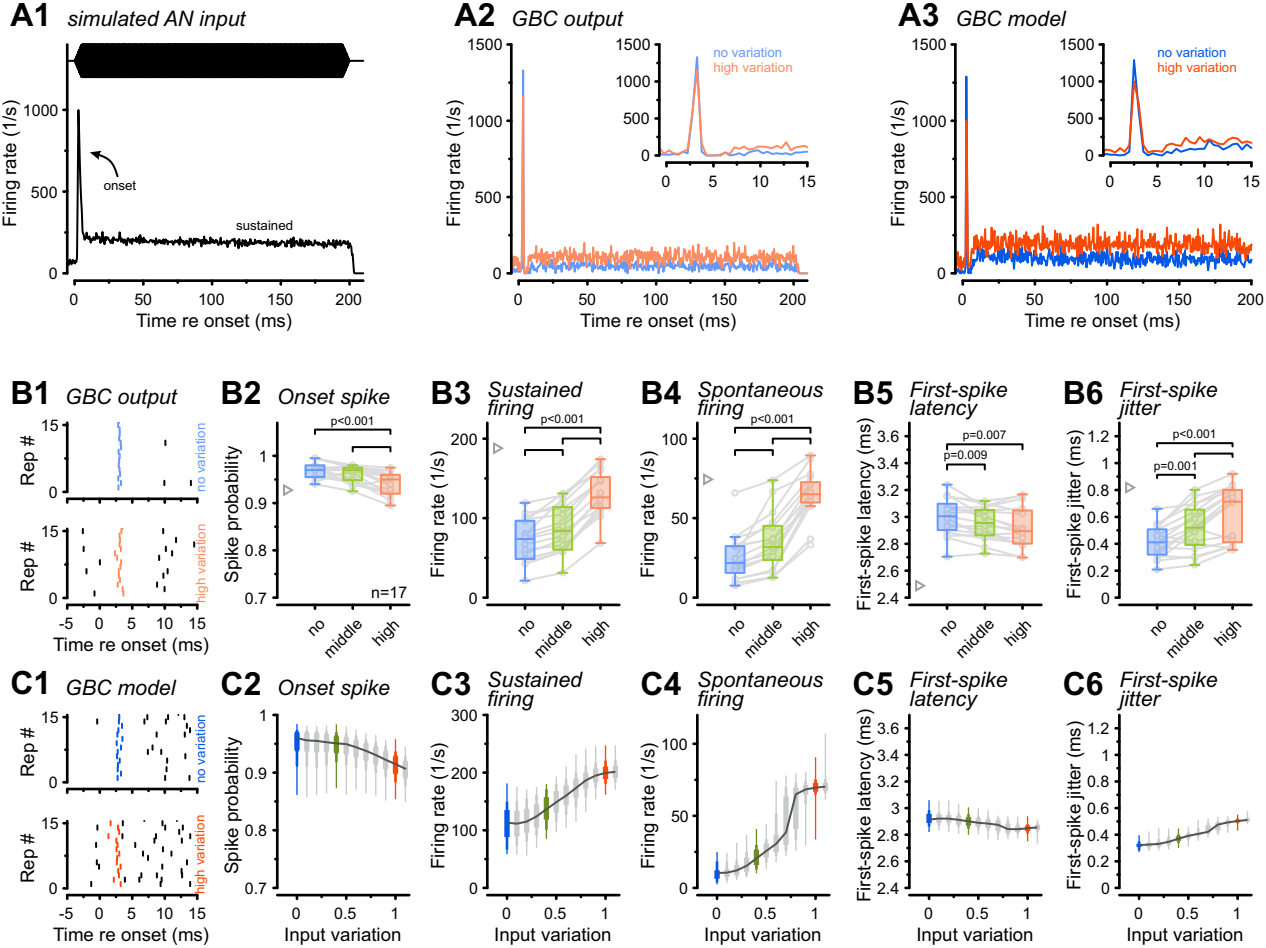
A1 simulated AN input
Firing rate (1/s)
onset
sustained
Time re onset (ms)
A2 GBC output
no variation
high variation
A3 GBC model
B1 GBC output
Rep #
no variation
high variation
B2 Onset spike
Spike probability
p<0.001
n=17
B3 Sustained firing
Firing rate (1/s)
B4 Spontaneous firing
B5 First-spike latency
First-spike latency (ms)
p=0.007
p=0.009
B6 First-spike jitter
First-spike jitter (ms)
p<0.001
p=0.001
no
middle
high
C1 GBC model
C2 Onset spike
C3 Sustained firing
C4 Spontaneous firing
C5 First-spike latency
C6 First-spike jitter
Input variation

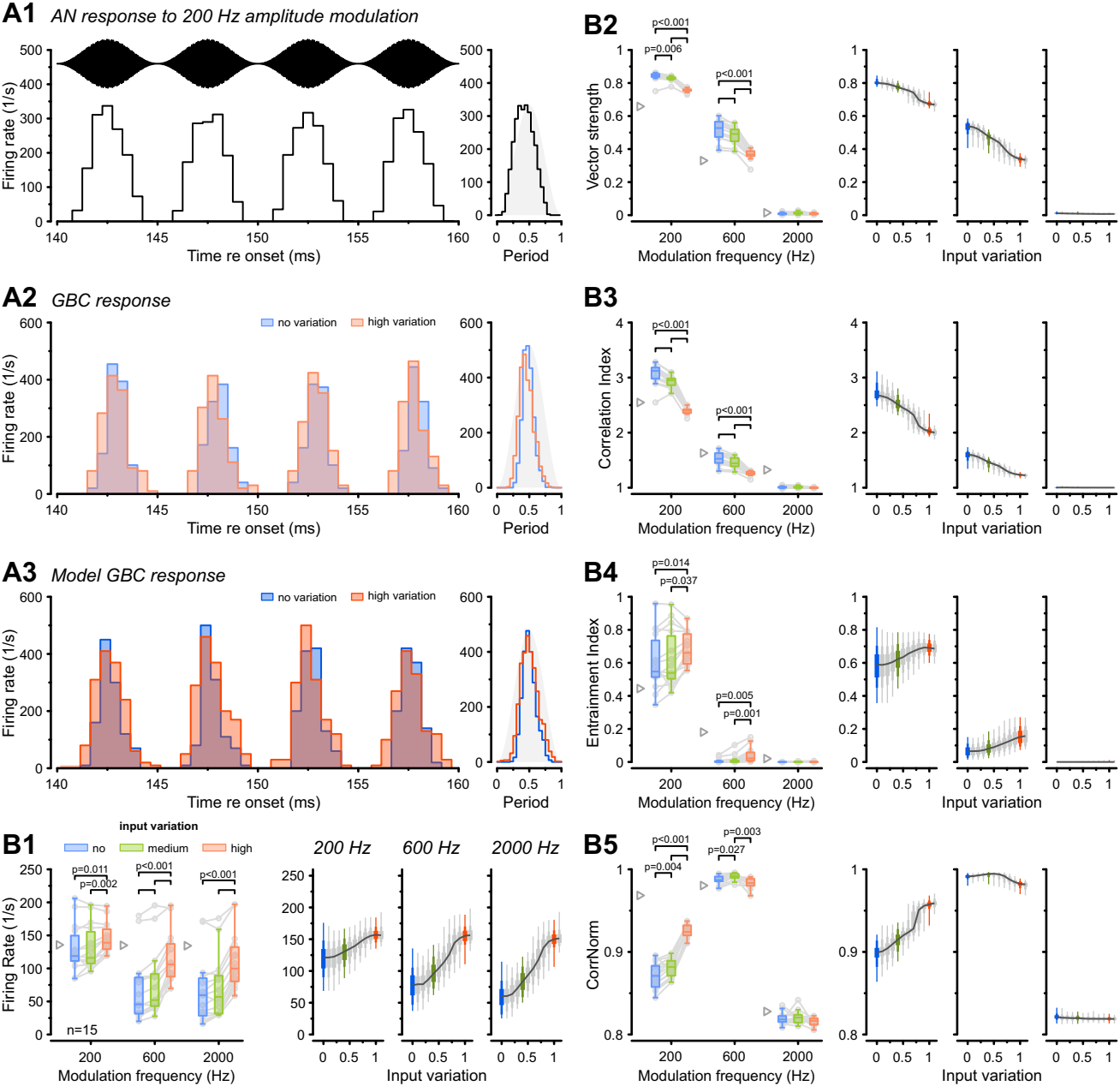
A1
AN response to 200 Hz amplitude modulation
Firing rate (1/s)
Time re onset (ms)
Period
B2
Vector strength
Modulation frequency (Hz)
Input variation
p<0.001
p=0.006
A2
GBC response
no variation
high variation
B3
Correlation Index
A3
Model GBC response
B4
Entrainment Index
p=0.014
p=0.037
p=0.005
p=0.001
B1
input variation
no
medium
high
200 Hz
600 Hz
2000 Hz
Firing Rate (1/s)
p=0.011
p=0.002
n=15
B5
CorrNorm
p=0.004
p=0.027
p=0.003

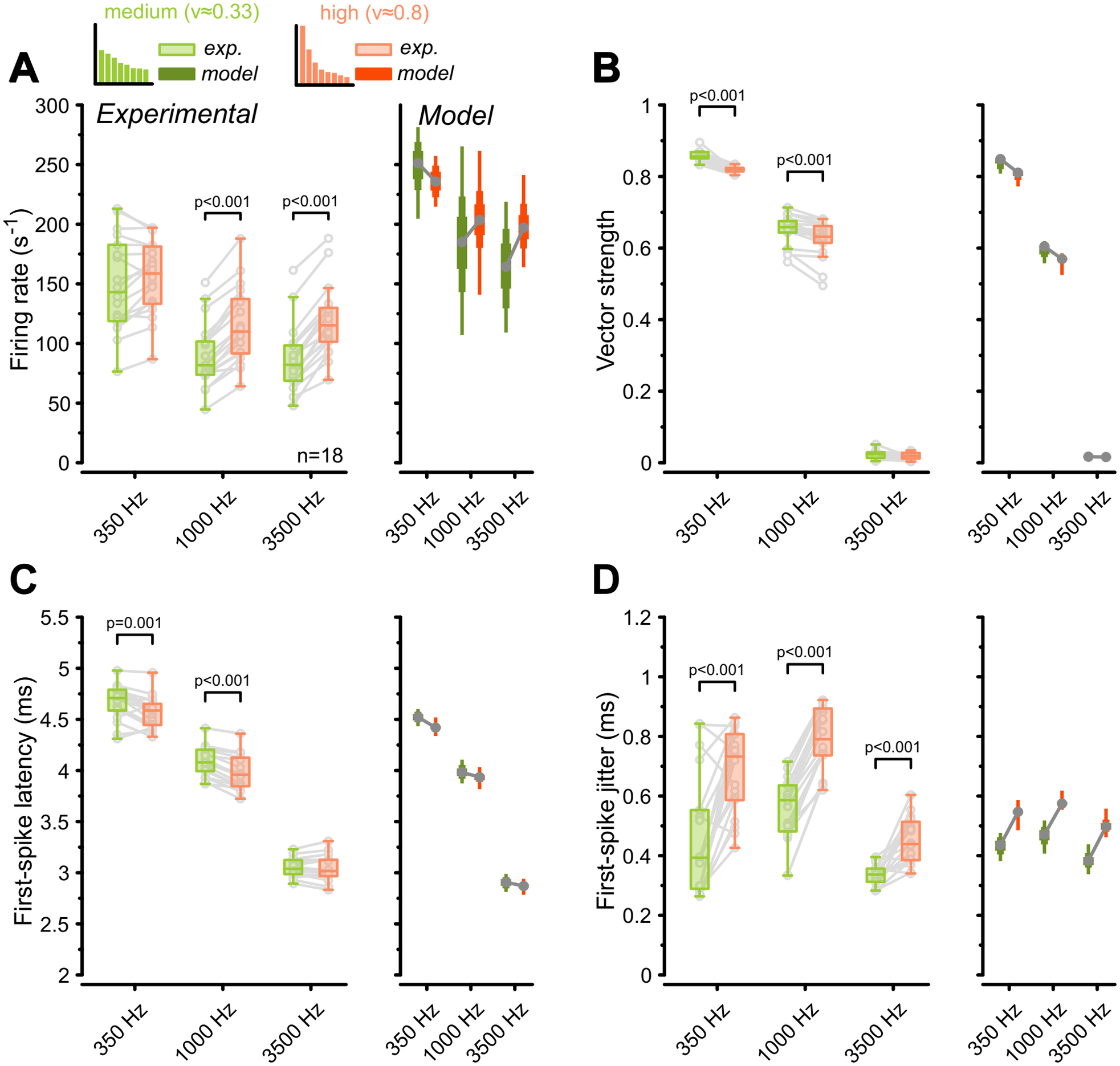
medium (v≈0.33)
high (v≈0.8)
exp.
model
exp.
model
A
Experimental
Model
Firing rate (s-1)
300
250
200
150
100
50
0
p<0.001
p<0.001
n=18
350 Hz
1000 Hz
3500 Hz
B
Vector strength
1
0.8
0.6
0.4
0.2
0
p<0.001
p<0.001
C
First-spike latency (ms)
5.5
5
4.5
4
3.5
3
2.5
2
p=0.001
p<0.001
D
First-spike jitter (ms)
1.2
1
0.8
0.6
0.4
0.2
0
p<0.001
p<0.001
p<0.001

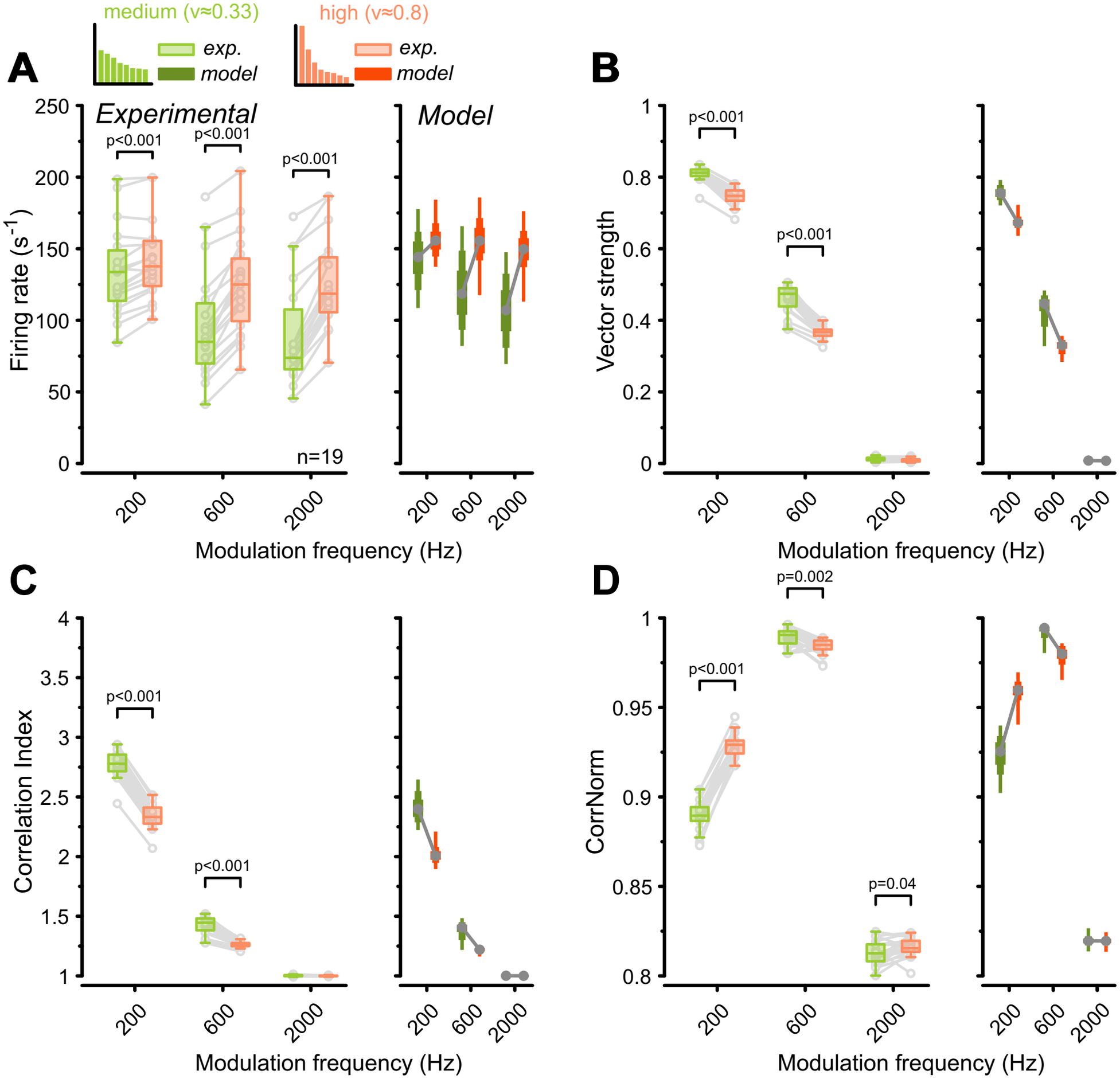
medium (v≈0.33)
exp.
model
high (v≈0.8)
exp.
model
A
Experimental
Model
Firing rate (s-1)
p<0.001
p<0.001
p<0.001
n=19
Modulation frequency (Hz)
B
Vector strength
p<0.001
p<0.001
Modulation frequency (Hz)
C
Correlation Index
p<0.001
p<0.001
Modulation frequency (Hz)
D
CorrNorm
p=0.002
p<0.001
p=0.04
Modulation frequency (Hz)